

Modeling the Optical Properties of Biomass Burning Aerosols: Young Smoke Aerosols From Savanna Fires and Comparisons to Observations from SAFARI 2000

R.I. Matichuk¹, P.R. Colarco², J.A. Smith¹, and O.B. Toon¹

¹Laboratory for Atmospheric and Space Physics, Department of Atmospheric and Oceanic Sciences, University of Colorado, Boulder, CO 80309

²Code 613.3, NASA Goddard Space Flight Center, Greenbelt, MD 20771

Annually, farmers in southern Africa manage their land resources and prepare their fields for cultivation by burning crop residual debris, with a peak in the burning season occurring during August and September. The emissions from these fires in southern Africa are among the greatest from fires worldwide, and the gases and aerosol particles produced adversely affect air quality large distances from their source regions, and can even be tracked in satellite imagery as they cross the Atlantic and Pacific Ocean basins. During August and September 2000 an international group of researchers participating in the Southern African Regional Science Initiative field experiment (SAFARI 2000) made extensive ground-based, airborne, and satellite measurements of these gases and aerosols in order to quantify their amounts and effects on Earth's atmosphere.

In this study we interpreted the measurements of smoke aerosol particles made during SAFARI 2000 in order to better represent these particles in a numerical model simulating their transport and fate. Typically, smoke aerosols emitted from fires are concentrated by mass in particles about 0.3 micrometers in diameter (1,000,000 micrometers = 1 meter, about 3 feet); for comparison, the thickness of a human hair is about 50 micrometers, almost 200 times as great. Because of the size of these particles, at the surface they can be easily inhaled into the lungs, and in high concentrations have deleterious health effects on humans. Additionally, these particles reflect and absorb sunlight, impacting both visibility and the balance of sunlight reaching Earth's surface, and ultimately play a role in modulating Earth's climate.

Because of these important effects, it is important that numerical models used to estimate Earth's climate response to changes in atmospheric composition accurately represent the quantity and evolution of smoke particles. In our model, called the Community Aerosol and Radiation Model for Atmospheres (CARMA) we used estimates of smoke emissions based on field studies and observations made with the NASA Terra and TRMM satellites. The meteorology used to calculate the transport was based on an assimilation of observed meteorological conditions provided by the National Center for Atmospheric Research. Our model was able to simulate much of the observed day-to-day variability in the smoke aerosol loading observed over the continent by the NASA AERONET network of ground-based sun photometers, suggesting that the observed variability is due more to meteorology than to day-to-day variability in emissions. We compared the simulated vertical profile of smoke concentrations with measurements made with NASA ground-based (MPLNet) and airborne lidars (Cloud Physics Lidar) and the NASA Ames

Airborne Tracking Sun Photometer and found that to a good approximation the smoke aerosols are emitted in a well-mixed layer near the Earth's surface called the planetary boundary layer. Because of the relative geographic sparseness of the AERONET, MPLNet, and airborne observations, it is important to also look at the observations made from satellites. Here we looked at observations of the smoke plumes made with the NASA MODIS, MISR, and TOMS satellite instruments, all of which provide important information about the quantity and distribution of aerosols present. These satellite instruments see the aerosols in somewhat complimentary ways, and we found important differences in their observed aerosol amounts, particularly over land, which highlights the difficulty in making these measurements. Overall, CARMA compared well with the observations available and we were able to constrain some of the parameters needed to accurately simulate the evolution of the optical properties of smoke aerosols as they are transported over long distances.

1 Modeling the Optical Properties of Biomass Burning Aerosols: Young Smoke Aerosols From
2 Savanna Fires and Comparisons to Observations From SAFARI 2000

3
4 R. I. Matichuk¹, P. R. Colarco², J. A. Smith¹, and O. B. Toon¹

5
6 ¹Laboratory for Atmospheric and Space Physics, Department of Atmospheric and Oceanic
7 Sciences, University of Colorado, Boulder, CO, 80309

8
9 ²NASA Goddard Space Flight Center, Code 613.3, Greenbelt, MD 20771

10
11 Corresponding Author: Rebecca I. Matichuk, University of Colorado, Boulder, Colorado, 80309,
12 303-492-3744 (Phone), 303-492-6946 (Fax), email: rebecca.matichuk@lasp.colorado.edu

Abstract

This study investigates the transport and optical properties of southern African biomass burning aerosols using an offline three-dimensional aerosol microphysical and transport model. Here we use Sun-photometer retrieved particle size distributions and monthly mean, satellite derived smoke emissions as input parameters in our model. We find that using these observations in our model allow us to reproduce the measured optical properties of smoke aerosols collected during the Southern African Regional Science Initiative campaign (SAFARI 2000). In particular, we find similar day-to-day oscillations in the simulated aerosol optical thickness (AOT) relative to AERONET measurements, suggesting that variations in aerosol loading are controlled more by transport processes than fluctuations in aerosol emissions. On a monthly basis, the model and observations from the MODIS, MISR, and EP-TOMS show that the dominant transport of smoke during September 2000 was westward towards the Atlantic Ocean. However, the observations show higher AOT values over the ocean than the model. These higher values observed by the satellites may be from the contribution of other aerosols or the condensation of gases onto the smoke, which are not simulated in this study. These higher values may also be a result of poor single scattering assumptions and/or the contamination of sub-pixel clouds in the satellite retrievals. At locations over Africa, we find discrepancies in AOT comparisons among the model and satellites which limits our ability in determining the performance of our model. We also suggest strategies for improving the treatment of particle size distributions of smoke aerosols in microphysical models.

36 Index Terms: 0305 Atmospheric Composition and Structure: Aerosols and Particles; 0312
37 Atmospheric Composition and Structure: Air/sea constituent fluxes; 0322 Atmospheric
38 Composition and Structure: Constituent sources and sinks; 0368 Atmospheric Composition and
39 Structure: Troposphere – Constituent transport and chemistry; 9305 Geographic Location:
40 Africa; Keywords: biomass burning smoke aerosols, transport model, biomass burning smoke
41 aerosol sources, smoke removal mechanisms.

1. Introduction

Biomass burning is a significant regional and global source of aerosols and trace gases [Crutzen and Andreae, 1990; Hao et al., 1990; Andreae, 1993]. The aerosols from both natural and anthropogenic burning of vegetation impact atmospheric chemistry, the radiation budget, air quality, and carbon cycling in ecosystems. It is now well known that biomass burning fires emit large amounts of carbon dioxide (CO_2), carbon monoxide (CO), nitrogen oxides (NO_x), methane (CH_4), nonmethane hydrocarbons (NMHC), oxygenated volatile organic compounds (OVOC), and reduced nitrogen-containing species (i.e., ammonia (NH_3) and hydrogen cyanide (HCN)) [Crutzen and Andreae, 1990 and Yokelson et al., 1996]. Some of these gases contribute to the greenhouse effect or are involved in photochemical processes that will generate greenhouse gases. In particular, biomass burning produces large amounts of CO (300 to $700 \text{ Tg(CO) yr}^{-1}$) and NO_x ($\sim 8 \text{ Tg(N) yr}^{-1}$), which are important precursors to the production of tropospheric ozone (O_3) [Seinfeld and Pandis, 1998]. Aerosols produced from biomass burning also influence the radiative properties of the atmosphere. Directly, biomass burning aerosols affect the radiation budget by scattering and absorbing shortwave (solar) radiation. Indirectly, these aerosols can serve as effective cloud condensation nuclei (CCN) at supersaturations greater than 0.5% which leads to the modification of cloud properties [Warner and Twomey, 1969]. IPCC [2001] provided a summary estimate that the global mean radiative forcing due to biomass burning aerosols is -0.2 W m^{-2} with an uncertainty as large as a factor of 3 and a “very low” level of scientific understanding. Additionally, satellites often observe smoke plumes being transported over intercontinental and continental scales, thereby degrading visibility not only at the smoke source but also downwind of the smoke source [Pósfai et al., 2003; Stein et al., 2003]. In particular, the Sea-viewing Wide Field-of-view Sensor (SeaWiFS) observed a significant smoke

event, now referred to as the “River of Smoke,” [Annegarn *et al.* 2002] where aerosols from biomass burning was transported over southern Africa and the Indian Ocean on 4 September 2000 as illustrated in Figure 1a.

Central and southern Africa experiences the most extensive biomass burning in the world [Scholes & Andreae, 2000]. It is estimated that approximately 49% of atmospheric carbon produced by fires worldwide comes from the savanna fires of Africa [Dwyer *et al.*, 2000; Scholes & Andreae, 2000] with emissions ranging from 80 to 785 Tg(C) yr⁻¹ [Scholes *et al.*, 1996, Barbosa *et al.*, 1999; van der Werf *et al.*, 2003]. There have been substantial scientific efforts at estimating smoke emissions, however the components (i.e., burned area, fuel loading, and combustion factors) used to calculate the emissions are highly uncertain producing values that fall within a large range.

The Southern African Regional Science Initiative campaign (SAFARI 2000) was an international scientific campaign to study land-atmosphere interactions in southern Africa during the wet season in 1999 and the dry season in 2000 [Swap *et al.*, 2003]. One of the main objectives of SAFARI 2000 was the characterization and quantification of regional emission sources from savanna burning using surface, aircraft, and remote sensing measurements of aerosol chemical composition, vertical distributions, refractive indices and particle size distributions. During the early part of the dry season in August, these fires were prescribed as a land management tool. The burning of wet soils at the beginning of the dry season produces low fire intensities, which result in limited vegetation consumption and limited damage to the soil. Farmers burn extensively in the early dry season to achieve rapid nutrient release prior to the new growing season and to stimulate regrowth of palatable grasses for their cattle. Early burning is also used in national parks as a preventative measure against late dry season fires, which tend

to be more intense and destructive. The estimated mean fire size, maximum fire size, and total burned area over Africa during the SAFARI 2000 campaign were 7.83 km², 1458 km², and 95,962 km², respectively [Hély *et al.*, 2003].

This paper focuses on modeling the transport and optical properties of biomass burning aerosols over continental Africa during SAFARI 2000. The optical properties investigated here include aerosol optical thickness (AOT), Ångström exponent (α), single scattering albedo (SSA) and vertical extinction profiles. Our first goal in this study is to determine suitable assumptions about aerosol emissions, injection altitudes, and initial particle size distributions that reproduce the observed optical properties of biomass burning aerosols. Our second goal is to better understand the microphysics needed to accurately simulate biomass burning aerosol properties. We conducted several simulations to investigate the model's sensitivity to: the timing and altitude of the smoke emissions; the transport of a particle size distribution; microphysical processes; removal schemes; and smoke optics. These sensitivity tests will aid us in understanding the parameters that control our model results.

Below, section 2 describes our model and input parameters used to simulate the biomass burning aerosols in our base simulation. Section 3 presents the results from our base simulation and sensitivity tests, and compares the results to observations made during SAFARI 2000. Lastly in section 4, we conclude with a discussion of the current ability to successfully model biomass burning aerosols produced from savanna fires over continental Africa.

2. Model Description

2.1 Dynamical Component

Our model is driven by meteorological fields derived from the National Center for Atmospheric Research (NCAR) Model for Atmospheric Transport and Chemistry (MATCH) [Rasch *et al.*, 1997]. MATCH is an offline chemical transport model that uses wind, temperature, and pressure fields provided by the National Center for Environmental Prediction (NCEP) reanalysis package (NCEP/NCAR reanalyses [Kalnay *et al.*, 1996]) and the physical parameterizations from the NCAR Community Climate Model version 3 (CCM3) [Kiehl *et al.*, 1996]. The NCEP/NCAR reanalyses are gridded at T63 horizontal resolution (approximately $1.875^\circ \times 1.875^\circ$) with 28 vertical sigma layers extending from the surface to approximately 35 km, and are available each day at 0000, 0600, 1200, and 1800 UTC. MATCH is run with half-hour timesteps, and the input fields are linearly interpolated to the current timestep. At each timestep MATCH employs the CCM3 physics to diagnose fields required to compute planetary boundary layer transport, convective mixing, and cloud and precipitation fields. We archive these fields every six hours for use in our aerosol microphysics and transport model. More details of our use of the MATCH derived fields are discussed in Colarco *et al.* [2003a].

2.2 Aerosol Transport Component

The global dynamical fields generated by MATCH are imported into our aerosol microphysical, transport, and radiation model, which is a version of the Community Aerosol and Radiation Model for Atmospheres (CARMA) developed at NASA Ames Research Center and the University of Colorado [Toon *et al.*, 1988; Ackerman *et al.*, 1995]. CARMA and MATCH have been previously applied to three-dimensional simulations of the transport and evolution of dust and carbonaceous aerosols [Westphal *et al.* [1991]; Colarco *et al.*, 2002; 2003a, b; 2004].

CARMA is a bin-resolving microphysical model that solves the aerosol continuity equation for source, transport, removal and transformation processes. The particle size distribution in CARMA is treated using a number of discrete bins distributed in radius space. In this study, the injected aerosols are distributed across 16 size bins spaced logarithmically between 0.01 μm and 10 μm radius sizes. For the smoke injection, we use a bimodal lognormal distribution based on observations (see section 2.6 and Figure 2). Additionally, only smoke aerosols are transported in the model (i.e., no dust or sea salt aerosols). The model can include all basic microphysical processes affecting aerosols; however in this study we only consider advection by winds, sedimentation, dry deposition, wet removal, coagulation, and prescribed aerosol sources. These processes are described in *Colarco et al.* [2003a]. Briefly, the advective and diffusive transports are solved using a mixed form of a numerically accurate, highly non-diffusive piecewise polynomial algorithm [*Collela and Woodward*, 1984] and a semi-lagrangian transport step following *Lin and Rood* [1996]. Particle transport by sedimentation and dry deposition are incorporated into the vertical transport component through fall velocities and deposition velocities, respectively. The fall velocity is computed for each size bin following the treatment by *Pruppacher and Klett* [1997]. The surface layer dry deposition velocity is calculated with a two-layer dry deposition model which accounts for sedimentation, molecular diffusion, and turbulent deposition across the lowest model layer [*Shao*, 2000]. CARMA's size-dependent, wet removal (scavenging by precipitation) parameterization uses the cloud and precipitation fields calculated in MATCH and is treated as a first order loss process as described by *Barth et al.* [2000]. The coagulation of the smoke aerosols is treated via Brownian motion. Here, our coagulation algorithm preserves the total aerosol volume but decreases the number concentration of particles as small particles stick together. In general, coagulation modifies the

particle size distribution by increasing the mean radius of the particle size distribution at a rate approximately proportional to the air temperature, the square of the particle number concentration, and the inverse of the particle radius.

For this study, CARMA is run at the same temporal and spatial resolution as MATCH, but on a limited area grid (180°W to 180°E and approximately 15°N to 60°S). The model is run for a number of simulations in order to test sensitivity to various parameterizations of sources and transport processes. The input smoke sources are calculated off-line, and are described in the next section. CARMA is driven for the period of August and September 2000 with half-hour timesteps. Here, the 6-hr input fields from MATCH are linearly interpolated to the desired timestep in CARMA. We include August to allow a 30-day spin-up time for aerosols in the model, and analyze only the September results.

2.3 Smoke Source Component

In this study, we are interested in testing how our modeled smoke fields compare to observations relatively near fire sources. The aerosol emissions used in the model were interpolated from the Global Fire Emissions Database (GFED), which provides a global 1° x 1° gridded monthly mean map of fire carbon consumption for the period January 1997 to December 2002 [van der Werf *et al.*, 2003]. The carbon consumed was constructed using the Tropical Rainfall Measuring Mission (TRMM) satellite and Visible Infrared Scanner (VIRS) hot spot data [Giglio *et al.*, 2002], Moderate Resolution Imaging Spectroradiometer (MODIS) burned area information [Kaufman *et al.*, 2003], and a spatially dependent relationship between fire counts and biomass consumed developed from the Carnegie-Ames-Stanford Approach (CASA) biogeochemical model. To convert carbon consumed due to fires into aerosol emissions for our

model we assumed an emission factor of 10.0 g Total Particulate Matter (TPM) per kg of Dry Mass (DM) [Sinha *et al.*, 2003], which is representative of savanna and grassland vegetation in Africa assuming 45% of the DM burned was carbon [Andreae and Merlet, 2001]. The smoke emissions are sensitive to the emission factor, and there are uncertainties in the GFED dataset particularly with relation to the burned area estimates [van der Werf *et al.*, 2003]. However, sensitivity simulations with other emission datasets (e.g., Korontzi *et al.* [2003], not shown) yield qualitatively similar spatial distributions of the smoke sources. We also assumed the fires emitted aerosol at the same rate each day. Over the approximately hemispheric domain of the model, the total aerosol emissions are about 4.52 Tg in August and 7.92 Tg in September, where approximately 2.14 Tg and 3.51 Tg of the total emissions were produced over Africa in August and September, respectively. Figure 3 shows the spatial distribution of aerosol emissions interpolated to our model grid over Africa for September 2000, and the African locations analyzed in this paper.

2.4 Smoke Optical Property Calculations

We calculated the AOT, SSA, Ångström exponent, and vertical extinction profile of our simulated smoke aerosol distributions using Mie theory [Wiscombe, 1979]. We represent the aerosols as spherical “smoke” particles, making no assumptions about their composition except their density (1.35 g cm^{-3} [Reid and Hobbs, 1998]) and their refractive index. We are not aware of any data suggesting that the SAFARI aerosols were external mixtures, so our approach is consistent with treating the aerosols as internal mixtures of absorbing and non-absorbing components. For simplicity, we selected a wavelength independent refractive index. The refractive index selected for the optical property calculations represents the mean complex

refractive index of days dominated by smoke aerosols at Ndola, Zambia for the month of September 2000 as retrieved by the Aerosol Robotic Network (AERONET) [Holben *et al.*, 1998] Sun-photometers (see Table 1 and Section 3.1.1 below). Our criterion for classifying smoke dominated days was based on an analysis of the AERONET climatology of cloud-screened, quality assured aerosol optical thickness for southern African observations. Here we found that the monthly mean AOT at 500 nm [AOT₅₀₀] exceeded 0.3 during months dominated by biomass burning emissions. Accordingly, when the daily average of AERONET observations show AOT₅₀₀ greater than 0.3, the day is classified as smoke dominated. Additionally, the humidification of the smoke aerosols was treated in the optical property calculations following a parameterization described by Magi and Hobbs [2003].

2.5 Base Model Description

The input parameters used in our base model are summarized in Table 1. In our base simulation, we assume the smoke particles have a lognormal size distribution using number fractions (N_f), geometric median radii (r_N), and standard deviations (σ) retrieved by an AERONET almucantar scan [Dubovik *et al.*, 2000] at Ndola, Zambia on 16 September 2000 (see location in Figure 3 and details in Table 1). We selected this particular particle size distribution because of the site's proximity to emission sources and because it has the highest daily mean AOT₅₀₀ of all the study sites in the smoke region during September 2000. This high optical depth suggests that it was dominated by locally generated smoke aerosols. Figure 2 (solid black line) presents the vertically column-integrated volume size distribution [$\mu\text{m}^3/\mu\text{m}^2$] used in the base model. It is not clear that the AERONET particle size distribution selected here represents young smoke (i.e., less than 3 minutes old [Haywood *et al.*, 2003]). Rather, it is likely more

representative of a mixture of young and moderately aged smoke, as well as contributions from other aerosols (e.g., dust), existing in different layers in the atmosphere. We find that a volume size distribution fit to parameters representative of young smoke (*Haywood et al.* [2003], grey dashed line in Figure 2) has a narrower fine mode volume size distribution than the AERONET retrieval, which suggests that the size distribution selected for our base model may not be representative of only young smoke. On the other hand, the coarseness of our model's spatial and temporal resolution prohibits a detailed treatment of truly fresh smoke aerosols. Therefore, the proximity of the Ndola site to emission regions suggests that this site provides a reasonable compromise between young and aged hazes at a scale our model can reasonably simulate.

Eck et al. [2003] observed significant diurnal variability in AOT_{500} over six sites in Zambia (Mongu, Ndola, Senanga, Mwinilunga, Zambezi, Solwezi) with a minimum AOT_{500} at 0900 UTC and maximum at 1500 UTC. For southern Africa, the TRMM satellite, which makes two overpasses every two days at the equator, also indicated a strong diurnal cycle in fire counts in August and September with a maximum number of fires occurring approximately 3 hours after local solar noon [*Giglio et al.*, 2003]. To represent a diurnal cycle in our base model, the aerosol emissions are concentrated during a 12-hour period between 0600 and 1800 UTC. Additionally, the smoke emissions are mixed throughout the depth of the planetary boundary layer to account for the convection and buoyancy associated with the heat and moisture in the fires [*Lioussé et al.*, 1996; *Lavoué et al.*, 2000]. The smoke emissions were evenly distributed between the surface model layer and model layer associated with the top of the planetary boundary layer (PBL) reported by MATCH. On average, the MATCH planetary boundary layer height (PBLH) at the six study sites was lowest between 0000 and 0600 UTC, with heights at approximately 0.3 km,

and peaked at 1200 UTC. The peak height of the MATCH PBL ranged between 1.5 km and 3.7 km.

3. Model Results and Discussion

The simulated optical properties are compared to satellite, aircraft and ground-based measurements made over southern Africa during September 2000. For this study, the model results are compared to data at six locations: Etosha Pan, Namibia; Inhaca, Mozambique; Mongu, Zambia; Ndola, Zambia; Senanga, Zambia; and Skukuza, South Africa (Figure 3). These locations were selected based on the amount of available data obtained during the SAFARI 2000 campaign and their proximity to aerosol source regions.

In section 3.1, we compare the results from the base model to observations made during SAFARI 2000, and discuss how well the initial input parameters used in our base model represent the aerosol distributions near the smoke source regions. Section 3.2 presents the results from a series of sensitivity tests to understand the influence the smoke source function and microphysical processes have on the model results.

3.1 Results – Base Model

3.1.1 Comparisons to Ground-Based Optical Measurements from AERONET

During SAFARI 2000, there were 17 Sun-sky photometer sites active in southern Africa as part of the globally distributed, federated Aerosol Robotic Network (AERONET) [Holben *et al.*, 1998]. The standardized AERONET instrumentation measures the direct solar beam transmission to determine the column-integrated AOT, and additionally retrieves water vapor, aerosol particle size distributions, and aerosol single-scattering albedo [Holben *et al.*, 1998;

Dubovik *et al.*, 2000]. In this study, we are using level 2.0 cloud-screened quality-assured data [Smirnov *et al.*, 2000]. The estimated uncertainty in AOT ranges between ± 0.010 and ± 0.021 , which is spectrally dependent with higher errors in the UV [Eck *et al.*, 1999]. The uncertainty in SSA is estimated to be ± 0.03 . The expected accuracy in the column-integrated volume size distributions are approximately 15-25% for radius sizes between $0.1 \mu\text{m}$ and $7 \mu\text{m}$ and 25-100% (or less than 10% of $dV/d(\ln r)$ in maximum) for sizes less than $0.1 \mu\text{m}$ and greater than $7 \mu\text{m}$ [Eck *et al.*, 1999; Dubovik *et al.*, 2000].

Figure 4 presents AERONET and simulated AOT₅₀₀ for each day in September 2000 at the six African study sites noted above. We point out that the AERONET measurements are essentially point measurements, while the resolution of our model grid box is approximately 200 km x 200 km. To make the model and measurements more comparable, we show all the retrievals made by AERONET (asterisks) in a single day and the daily mean AOT₅₀₀ simulated by the model. The solid line represents the results from the base model, and the dashed line represents the results from a simulation where we generated variable emissions on a daily basis (see Section 3.2). Qualitatively, we find that simulated AOT₅₀₀ falls within the daily range of AERONET retrievals on most days, and illustrates a similar temporal variation. The day-to-day fluctuations in the simulated AOT₅₀₀ are remarkable given the fact that the emissions used in the model are released at a constant rate for the month of September. This suggests that the oscillations in the simulated AOT₅₀₀ are controlled more by the variability in the meteorological conditions than the temporal and spatial variations in the fire activity. This has also been observed by Myhre *et al.* [2003]. On days when the model does not agree with AERONET, the model is generally underestimating the daily mean AOT₅₀₀. However, at Etosha Pan we do find that the model overestimates the daily mean in the latter half of the month.

We also find that the timing and magnitude in the simulated AOT₅₀₀ compares better to AERONET at Etosha Pan, Inhaca, Ndola, and Skukuza than at Mongu and Senanga. Although the model AOT₅₀₀ does not correlate well with the AERONET observations at Mongu and Senanga, it is interesting to note that the model AOT₅₀₀ at Mongu is well correlated with the model AOT at Senanga. This is not necessarily surprising since the two sites are within a couple of hundred kilometers of each other (i.e., adjacent grid cells). However, the fact that the AERONET observations at the two sites are also well correlated with each other suggests that the aerosol loading at both locations is affected by dynamical and emission processes happening on synoptic rather than local scales. MODIS (AOT₅₅₀) retrievals from 4 – 6 September and 15 – 17 September (not shown) confirm the large-scale aerosol loading, where it shows AOT₅₅₀ values greater than 1.0, presumably associated with biomass burning, over a large portion of Zambia which encompasses both of these sites. Comparing the MODIS observations on these days to the model results (not shown) reveals that the model has the plume in the correct location during the 4 – 6 September but underestimates the AOT relative to MODIS. However during the 15 – 17 September, the model plume is placed too far south relative to MODIS, thereby causing poor correlations between the model and AERONET during this period. These results suggest a problem with the model dynamics during this period, although it does not rule out that there may be a major and perhaps episodic aerosol source not in the GFED dataset.

Figures 5 – 7 present scatterplots of simulated and AERONET daily mean AOT₅₀₀, SSA₄₄₀, and Ångström exponent [$\alpha_{440/870}$] on smoke dominated days at all six study sites, respectively. The correlation coefficient (R) and the equation of the line of best fit are also reported in each scatterplot. Although the model AOT is well correlated with the AERONET observations (R=0.78, Figure 5), we find that the model underestimates the daily AOT₅₀₀ by up

to a factor of 2 when AERONET retrievals are greater than 1.0. This may be a result of spatially small, dense aerosol plumes observed by AERONET which cannot be resolved in our model. When we discard the AERONET observations greater than 1.0, we find that the correlation coefficient increases to 0.81 and the slope of line of best fit is closer to 1 (slope = 0.80). In the comparisons of daily SSA_{440} and Ångström exponent, we find that the model results do not show as much variability as the AERONET retrievals (Figures 6 and 7, respectively). Here the simulated SSA_{440} ranges between 0.85 and 0.90, where the AERONET retrievals range between 0.85 and 0.95. Given the large uncertainty in the AERONET SSA retrievals (i.e., ± 0.03 and represented by single bar at top-left corner of Figure 6), the model is within the measurement error for SSA. The simulated Ångström exponent ranges between 1.70 and 1.95, where the AERONET retrievals range between 1.40 and 2.10. This difference suggests that our model is not capturing the variability in the size distribution correctly. The model results may be improved if we consider the condensation of gases onto the smoke aerosols, and the contribution from other aerosol species that exist at these study sites (i.e., Aeolian dust, sea salt, and fossil fuel combustion). The model's sensitivity to initial size distribution will be discussed further in section 3.2.

Figures 8 and 9 compare the monthly mean spectral dependence of AOT and SSA (i.e., how AOT and SSA changes with wavelength) of smoke dominated days for September 2000, respectively. The asterisks connected with a dashed line represent the AERONET data and the solid line represents the results from the base model. For the remaining portion of this paper, we only discuss the results from Ndola and Inhaca since we find similar results at the other sites. Etosha Pan, Mongu, and Senanga comparisons are similar to the results found at Ndola, while the Skukuza comparison is similar to the results found at Inhaca. At Inhaca and Ndola, we find

that the mean wavelength dependence of AOT simulated by the base model is similar to the wavelength dependence retrieved by AERONET. The maximum difference between the model and AERONET monthly mean AOT at all measured wavelengths is approximately 30% at both sites. We find that the simulated wavelength dependence of SSA is comparable to AERONET at Ndola but not at Inhaca. At Inhaca, we find that the simulated monthly mean SSA is within the uncertainty of the AERONET retrievals at wavelengths less than 870 nm. However, at wavelengths greater than 870 nm, the model overestimates the absorption by approximately 50%. Again, this suggests that our model is not capturing the variability in the size distribution and/or refractive index correctly. Also note that the SSA is wavelength dependent. Here we find that it is larger at shorter wavelengths for both the model and the data despite the refractive index for the model being assumed to be wavelength independent. Further investigations of wavelength independent and dependent refractive indices are discussed in section 3.2.

The spectral dependence of the AOT lends important insight into the size distribution of particles being considered. Using AERONET data, *Eck et al.* [1999] characterized the spectral properties of African and South American biomass burning aerosols. A typical method of inferring particle size information from Sun-photometer observations is to compute the Ångström exponent (α), which requires the AOT retrieval at two wavelengths (see *Eck et al.* [1999], equation 2) and represents the first derivative of the variability of $\log_e(\text{AOT})$ versus $\log_e(\text{wavelength})$. As defined, Ångström exponent values near 2.0 correspond to measurements that are dominated by small-sized particles (i.e., smoke aerosols), while values near 1.0 correspond to large-sized particles (i.e., dust and sea salt). Since the major contribution to AOT for biomass burning is from sub-micron, accumulation mode size particles, *Eck et al.* [1999] recommend that the Ångström exponent be computed from shorter wavelength pairs which have

much greater sensitivity to accumulation mode size particles than from longer wavelength pairs. To acquire information about the relative contributions of the accumulation and coarse mode particles to the total AOT, *Eck et al.* [1999] also recommend computing a curvature term (α') which provides information on the second derivative of the $\log_e(\text{AOT})$ versus $\log_e(\text{wavelength})$ relationship. As defined in *Eck et al.* [1999], equation 8, larger (positive) values of the curvature term indicate relatively larger contributions of accumulation mode versus coarse mode particles to the total AOT. For biomass burning aerosols in Mongu, Zambia, *Eck et al.* [1999] find $\alpha = 1.21$ for the 380 nm and 440 nm wavelength pair and a curvature value of $\alpha' = 1.24$.

Table 2 lists the monthly mean AOT_{500} , $\alpha_{380/440}$, α' , SSA_{440} , SSA_{670} , SSA_{870} , and SSA_{1020} of smoke dominated days at Inhaca and Ndola. To compute the derivative of the Ångström exponent (α'), we used wavelengths at 380, 500, and 870 nm. The AERONET observations at both locations show similar Ångström exponent values, which for this short-wavelength pair indicate similar fine mode sizes, but very different curvature values. The slightly lower Ångström exponent and much lower curvature value at Inhaca relative to Ndola is consistent with the known contribution of coarse mode aerosols at this location [*Eck et al.*, 1999], while the Ndola observations are more consistent with a biomass burning dominated site. The base model results at both locations are similar to each other, and the model agrees reasonably well with the observations at Ndola, but underestimates the coarse mode contribution to the AOT at Inhaca. The fact that the model underestimates the coarse mode contribution to AOT at Inhaca is not surprising since we are not simulating the sea salt and dust aerosols, which is likely to explain the observations. As shown in Figure 9 and reported in Table 2, the model is slightly less absorbing at Ndola and slightly more absorbing at Inhaca compared to AERONET. However, the model SSA is within the uncertainty of the AERONET retrieval error bars at all wavelength

retrievals, except for the 1020 nm wavelength retrieval at Inhaca. The 1020 nm retrieval may be understood as due to the coarse mode aerosols explained above.

3.1.2 Comparisons of Vertical Extinction Profiles from Airborne and Ground-Based Measurements

During SAFARI 2000, the NASA 14-channel Ames Airborne Tracking Sun-photometer (AATS-14) was operated aboard the University of Washington's Convair-580 research aircraft [Schmid *et al.*, 2003]. The AATS-14 made measurements of smoke originating from flaming grass fires occurring at several locations in central and southern Africa. The AATS-14 measured the transmission of the direct solar beam for 14 discrete wavelengths from 354 nm to 1557 nm from which the spectral AOT can be derived. In general, the AATS-14 profiles showed that most or all of the aerosols were below 4 km with extinctions at 525 nm as large as 0.35 km^{-1} during the SAFARI 2000 campaign [Schmid *et al.*, 2003]. Depending on synoptic conditions, some profiles showed multiple-layers, where an aerosol layer would be present between the surface and approximately 1.5 km and an additional layer between 2 km and 4 km [Schmid *et al.*, 2003].

The Cloud Physics Lidar (CPL) also made measurements during the SAFARI 2000 campaign. The CPL was built for use on the NASA ER-2 high-altitude aircraft. This instrument provides information on cloud height and structure as well as aerosol optical thickness, and operates simultaneously at 3 wavelengths: 355 nm, 532 nm, and 1064 nm [McGill *et al.*, 2003]. The CPL fundamentally measures range-resolved profiles of volume 180-degree backscatter coefficients, with a vertical resolution fixed at 30 m. During SAFARI 2000, the CPL profiles showed that most of the aerosols were below 4 km with extinctions at 532 nm as large as 0.8 km^{-1} [McGill *et al.*, 2003].

The Micro-Pulse Lidar (MPL) was also operational during the SAFARI 2000 field campaign [Spinhirne *et al.*, 1995]. The MPL is a single channel (523 nm), autonomous, eye-safe lidar system originally developed at the NASA Goddard Space Flight Center. Several instruments are collocated with AERONET Sun-sky radiometers as part of a global lidar network (MPLNET, Welton *et al.*, [2001]). The MPL is used to determine the vertical structure of clouds and aerosols to produce optical properties, such as extinction and optical depth profiles of the clouds and aerosols. The MPL profiles at multiple African locations generally showed most of the aerosols below 4 km with extinctions at 523 nm as large as 0.3 km^{-1} .

Figure 10 compares the simulated mean vertical extinction profiles at 525 nm to measurements collected by the AATS-14 and CPL at comparable wavelengths (i.e., CPL at 532 nm) at Mongu and Senanga, Zambia on 6 September 2000. In this figure, the simulated mean extinction profiles represent the average model results at 0600 and 1200 UTC, the CPL profiles represent the average of four samples taken between 0800 and 1100 UTC (black lines), and the AATS-14 profiles represent a single sample (red lines). The blue lines are the results from the base model, and the green lines are results from a sensitivity study testing different injection height strategies (see Section 3.2). In general, we find that the results from the base model compare well to the observations at the selected African locations. Again, we find similarities in the simulated and observed vertical profiles at both sites which may be associated with a large-scale smoke event. However, the AATS-14 measurement observes a well defined smoke layer between 2 km and 4 km where the base model does not. This may be a result of excess mixing in our model, which is possibly related to the excessively coarse vertical resolution in the model. It is however difficult to draw conclusions about the behavior of the model from single smoke

events such as these aircraft samples since they may have detected isolated plumes on a scale much smaller than the model resolution.

Figure 11 compares the simulated mean vertical extinction profile at 525 nm to the mean MPL measurements at 523 nm at Skukuza, South Africa. We are using level 1.5a data products from MPL (real-time cloud and aerosol data). The computed mean includes all days when MPL was operational (i.e., 1-3, 6, 7, 9, 10, 13, 14, 17 September 2000). The dashed line represents the MPL measurements and the remaining lines represent the results from various model simulations. In this section, we are only concerned with the solid black line which represents the results from the base model. Here we find that the base model results compare very well to the MPL measurements.

3.1.3 Comparisons to Spaceborne Measurements of Aerosol Optical Thickness

Figure 1b shows the simulated daily mean AOT at 550 nm on 4 September 2000, the same day as the SeaWiFS satellite image shown in Figure 1a. Here we find that the model produces a similar pronounced aerosol transport corridor across southeastern Africa and over the Indian Ocean or the “River of Smoke”. Qualitatively, this simple comparison demonstrates our model’s capability of transporting smoke aerosols properly on a single day.

Figures 12 – 14 compare the simulated monthly mean AOT from the base model to the retrieved AOT from polar orbiting satellite platforms: the Moderate Resolution Imaging Spectroradiometer (MODIS) [Kaufman *et al.*, 1997; Tanré *et al.*, 1997], the Multiangle Imaging Spectroradiometer (MISR) [Diner *et al.*, 1998; Martonchik *et al.*, 1998, 2002], and the Total Ozone Mapping Spectrometer onboard the Earth Probe satellite (EP-TOMS) [Torres *et al.*, 1998], respectively, over southern Africa for September 2000. MODIS and MISR are both flying

on the NASA Terra spacecraft, with an equator crossing time of approximately 10:30 AM and 10:30 PM local time. Both instruments therefore have similar temporal coverage, although their fields of view are somewhat different, reflecting the different capabilities of each instrument. The EP-TOMS instrument has equator crossing times of about 10:00 AM and 10:00 PM local time. For all three instruments only the day-lit observations are useful for obtaining AOT retrievals. From theoretical sensitivity studies, the estimated uncertainty in the AOT for MODIS is the larger of ± 0.05 and $[\pm 0.2AOT_{550}]$ over land and ± 0.03 and $[\pm 0.05AOT_{550}]$ over ocean [Kaufman *et al.*, 1997; Tanré *et al.*, 1997], for MISR it is the larger of ± 0.05 and $[\pm 0.2AOT_{550}]$ over the land and ocean [Kahn *et al.*, 2001], and for EP-TOMS it is the larger of ± 0.1 and $[\pm 0.3AOT_{500}]$ over land and ocean [Torres *et al.*, 1998].

In order to quantitatively compare the satellite retrievals to our model we developed an *ad hoc* aggregation and sampling strategy for computing the monthly mean of the satellite retrieved AOT. The retrievals are typically available at a much higher spatial resolution than our model: $10 \times 10 \text{ km}^2$ for MODIS, $17 \times 17 \text{ km}^2$ for MISR, and approximately $24 \times 24 \text{ km}^2$ for EP-TOMS. These are commonly referenced as “Level 2” products. The various satellite retrievals are also generally available in a gridded (“Level 3”) product which typically has a $1^\circ \times 1^\circ$ spatial resolution, but the quantitative validity of these products when used to construct a monthly mean can be slightly dubious in situations where only a few number of pixels (others being cloud- or glint-obscured) dominate the monthly mean. For this reason, our goal in this section is to develop a method to quantitatively compare the satellite retrievals to our model and the satellites to each other by constructing our own gridded product from the Level 2 retrievals.

Our approach was to first aggregate the retrievals at their native resolution to our model grid for each day, eliminating all but the highest quality pixels (based on quality assurance flags

or other information associated with the retrieval product). This way we find the average retrieved AOT in each model grid box on each day, as well as the number of retrievals available and the standard deviation about the mean. The monthly mean at each grid box was constructed from the daily averaged grid box values, but only using days which exceeded some threshold number of valid retrievals (the pixel threshold, eliminating grid boxes which are dominated by only a few retrievals). The pixel threshold value is a function of the satellite instrument (i.e., we require more pixels for the high resolution MODIS and fewer for the low resolution TOMS) and the satellite repeat cycle (near daily coverage for MODIS versus the 7 – 8 day repeat cycle for MISR). The monthly mean at each grid box is then the mean of the daily values passing the pixel threshold test, weighted by the number of pixels per day. This strategy is applied in an *ad hoc* manner in the sense that we selected each satellite's pixel threshold by iteration, selecting where small variations in the pixel threshold did not lead to significant changes in our computed monthly mean. Accordingly, the pixel threshold for each sensor is: 15 for MODIS, 5 for MISR, and 3 for EP-TOMS. Finally, the model AOT was sampled near the satellite overpass time and only where the satellite daily grid box averages passed the pixel threshold test. The model monthly mean was then constructed by weighting it in the same fashion as the satellite monthly mean. Thus, for each satellite we have a unique monthly mean of the model AOT which can be compared to the satellite retrieval at the model resolution.

To assess our sampling and aggregation method, we compared our MODIS results to the MODIS Online Visualization and Analysis System (MOVAS) product (not shown) (<http://g0dup05u.ecs.nasa.gov/Giovanni/>) and found that the patterns in the monthly mean AOT are qualitatively consistent between the two products. While we have not fully evaluated this technique, it addresses the non-trivial problem of scaling and aggregating high resolution

satellite observations for quantitative comparisons to relatively coarse resolution simulations. Our work here is ongoing [Colarco *et al.*, in preparation, 2006].

Qualitatively, the satellites (Figures 12 – 14) all show a similar aerosol feature over the same portion of southern Africa and eastern Atlantic Ocean (from approximately 0° to 30°S and 12°W to 40°E). Over land, we find that the peak mean AOT observed by the satellites is further north and east (southwestern Zaire) relative to the base model (northeastern Angola). Over the ocean, we find that all the satellites detect higher monthly mean AOT values over the eastern Atlantic Ocean (approximately 5°S to 15°S and 0° to 15°E) relative to the base model. Despite differences in magnitude, the model agrees with the satellite retrievals in the general placement of the smoke plume. The hatched marks in Figures 12 – 14 represent locations with “No Data” (N.D.) or locations that did not pass the sampling requirements discussed above. MISR and EP-TOMS have more locations with no observations than MODIS which may be a result of the temporal and spatial coverage (i.e., larger pixel size) of each satellite.

To quantitatively compare the satellite observations to the model, Figures 15 – 17 show scatterplots of the satellite versus model monthly mean AOT shown in Figures 12 – 14. Here we separate the comparison by land and ocean points. This division is particularly relevant for MODIS, which explicitly uses a different inversion algorithm over land than over ocean, but it also lets us compare the MISR and EP-TOMS performance over these two different surface classifications. The dashed lines represent the 1-to-1 line and the solid lines represent the line of best fit. The correlation coefficient (R), the equation of the line of best fit, and the number of locations (listed in parentheses) are also reported in each scatterplot. For clarity, we grouped the uncertainty in the data into intervals of 0.2. Here, the error bars represent the average uncertainty in the data at each interval. In general, we find that our model results are linearly correlated to

the satellite observations, with stronger correlations over the ocean. Additionally, we find that the model has lower AOT values compared to all the satellite products, with larger disagreements in the ocean comparisons. Over land, we find that the model and MISR agree the best with the strongest correlations and slope nearest to 1. However over the ocean, we find that the model agrees best to MODIS. We also find the largest disagreement between the model and EP-TOMS AOT over the ocean (i.e., weak correlation and significant offset in the slope of the line of best fit) which may be a result of the assumptions being made in the EP-TOMS retrievals. In particular, unfiltered sub-pixel clouds may be contributing to the larger AOT signal.

There are at least three issues that could explain the model's lower AOT values over the ocean. First, our sampling and aggregation strategy incorporated fewer pixels in a model grid box per day over the ocean than land due to sunglint (particularly in MODIS retrievals) and persistent cloud cover in certain regions, so we may be biased in that regard. Over land the average number of pixels in a model grid box per day during September 2000 was: 107 for MODIS, 48 for MISR, and 9 for EP-TOMS; while over the ocean: 84 for MODIS, 40 for MISR, 8 for EP-TOMS.

Second, the model may be deficient in that we are neglecting other important aerosol species, such as sea salt and dust. The mean Ångström exponent at the 470/670 nm wavelength pair retrieved by MISR and MODIS during September 2000 over this region ranged between 0.2 and 1.4. These values are commonly associated with large particles suggesting that dust and sea salt aerosols may be contributing to the higher AOT values, which would not be seen by our model since we are not simulating these aerosols. In addition, the model may not be properly accounting for significant microphysical evolution of smoke particles through, for example,

condensation of gases within the smoke plume, or the humidification of the smoke aerosols (discussed in more detail in section 3.2).

A third point is that the high monthly mean AOT values detected by the satellite instruments over the Atlantic Ocean may be due to complications and/or errors in the satellite retrievals. A study completed by *Ichoku et al.* [2003] suggested that the global constant SSA of 0.90 at visible wavelengths assumed in the smoke aerosol retrievals by MODIS is too high. Rather a SSA of 0.86, or smaller for fresh smoke aerosols, is more representative of biomass burning aerosols over southern Africa. Additionally, it is known that this region of the world has persistent, extensive stratus decks. The mean reflectivity from EP-TOMS for September 2000 indicates high levels of reflectivity (~25 to 50%) over this region suggesting that unfiltered sub-pixel clouds may be contributing to the high AOT feature over the Atlantic Ocean.

Since we observe inconsistencies in the comparisons between the model results and satellite observations, we compared MODIS to MISR (Figure 18). Figure 18 scatters the monthly mean AOT₅₅₀ of MODIS versus MISR at the model resolution over the land and ocean. The monthly mean of the MISR and MODIS data was calculated by first aggregating the Level 2 products to our model grid for each day using the same pixel thresholds discussed above. The monthly mean at each grid box was then constructed from the daily averaged grid box values where both MODIS and MISR made retrievals. The correlation coefficient (R), the equation of the line of best fit, and the number of grid points (listed in parentheses) are reported in each scatterplot. Again, the error bars represent the average uncertainty in the data at each interval of 0.2. In general, we find that the datasets compare well over land and ocean with high correlations, low offsets and slopes near 1. However, MISR is lower than MODIS by approximately 25% over land and approximately 10% over the ocean. *Abdou et al.* [2005] found

566 similar comparisons between MISR and MODIS data collected during three months of 2002
567 (March, June, and September). Since the satellite AOT observations are in good agreement over
568 the ocean, the model is most likely missing information about the aerosols. However, the
569 disagreement in the satellite AOT observations over land does not provide us with enough
570 information to determine if the model is quantitatively doing a poor job.

571 To better understand the model's capability over land, we compared the simulated mean
572 AOT to MISR, MODIS, and AERONET at the six study sites (Table 3). Note the satellite
573 instruments should not be compared to AERONET quantitatively in this case since they have
574 been degraded to our model resolution. Direct comparison of the satellite to AERONET is more
575 correctly done using the higher resolution Level 2 products and examining the temporal
576 correlation between the satellite and AERONET observations (e.g., as was done for MODIS in
577 *Ichoku et al.* [2003]). Table 3 shows the simple mean of all days in the month where the MISR,
578 MODIS, and AERONET datasets overlap, with AERONET and the model sampled as close to
579 the satellite overpass time as possible. For AERONET, the mean represents the average of
580 retrievals made within an hour of Terra's overpasses time (i.e., between 800 UTC and 1000
581 UTC), while the model average represents the results at 1200 UTC. Here we find that the model
582 compares best to MISR at four of the six study sites (Etosha Pan, Mongu, Ndola, and Senanga)
583 and compares best to MODIS at the remaining two sites. However, the model is consistently
584 higher than MISR and lower than MODIS. Compared to AERONET, the model is lower at all
585 sites except at Skukuza. Additionally, we find that MISR AOT is always lower than MODIS
586 AOT. As noted above in section 3.1.1, we found that the optical properties at both Inhaca and
587 Skukuza were different from the other sites since they are influenced by other aerosol sources
588 (i.e., dust and sea salt). Therefore, we find it interesting that the model compares best to MODIS

at Inhaca and Skukuza, whereas the sites that are more clearly dominated by smoke compare better to MISR. Since the model behaves essentially the same at all sites, this discrepancy in the comparison of MODIS and MISR probably reflects the differences in the retrieval techniques. This relationship may suggest that MISR is less sensitive to coarse mode particles, such as the aerosols found at Inhaca and Skukuza, while MODIS is not. These results may also suggest that the algorithms used by MISR may be more appropriate for retrievals that are dominated by a single aerosol source, where the MODIS algorithms may be more appropriate for retrievals with multiple aerosol sources.

Since the EP-TOMS AOT is only provided at 380 nm, we constructed Table 4 to compare the model to the EP-TOMS and AERONET observations at the six study sites. Again to be consistent in the comparisons, the mean only includes days when all the instruments made retrievals, with AERONET and the model sampled as close to the satellite overpass time as possible. For AERONET, the mean represents the average of retrievals made within an hour of the Earth Probe's overpass (i.e., between 930 UTC and 1130 UTC), while the model mean represents the results at 1200 UTC. Here we find that the model mean AOT_{380} compares best to AERONET at four of the six study sites (Etosha Pan, Inhaca, Senanga, and Skukuza). However the model has lower mean AOT_{380} values at all sites except at Inhaca. We also find that the model is either higher or lower relative to the EP-TOMS mean values at the selected study sites.

In this section we developed a method for quantitatively comparing the satellite retrieved AOT to the model. In general, we find that the model underestimates the AOT relative to all the satellite datasets. The model agrees best with MISR over land, MODIS over the ocean, while agrees the least with EP-TOMS AOT retrievals over both land and ocean. We also find that MODIS and MISR agree better over the ocean than over the land, despite them observing the

same scenes. These results may reflect the strengths and weaknesses of each satellite. A general problem found with all satellite sensors is sub-pixel cloud contamination, and is perhaps the worst with EP-TOMS because of its large pixel size. The better agreement between MODIS and MISR over the ocean suggests that the satellite algorithms use similar assumptions to retrieve the AOT. As Figure 18 indicates and noted in Table 3, MODIS and MISR do not agree with each other over the land, and the model AOT compares better to MISR at Etosha Pan, Mongu, Ndola, and Senanga but better to MODIS at Skukuza and Inhaca. In the context of the AERONET observations we have already found that Skukuza and Inhaca are influenced by multiple aerosol sources and characterized by having more coarse mode aerosols than the other sites. This suggests that the various satellite retrieval algorithms have divergent capabilities in detecting the variability in the aerosol optical properties across the six land sites explored here. Over land sites dominated by fine mode aerosols, presumably smoke aerosols, we might reasonably expect more confidence in the MISR retrieval because of fewer assumptions on the behavior of the surface reflectance characteristics. However at land sites with multiple sources of coarse mode aerosols, most likely dust and sea salt aerosols, we might expect more confidence in MODIS because of its wider spectral range. In the end, the discrepancies between the satellites over land mean that it is unclear how well the model is really doing. Over the ocean, the better agreement between MODIS and MISR and the consistently smaller AOT in the model relative to those sensors suggests important contributions from other aerosol sources which are being neglected in the current version of the model.

3.1.4 Comparisons to EP-TOMS Aerosol Index

In this section, we compare the results from the base model to the aerosol index (AI) retrieved by EP-TOMS for September 2000 [Torres *et al.*, 1998]. Briefly, the AI is a measure of the wavelength-dependent reduction of scattered radiance by aerosol absorption relative to a pure Rayleigh scattering atmosphere. The aerosol index is defined so that positive values generally correspond to UV-absorbing aerosols and negative values correspond to non-absorbing aerosols. However, when absorbing aerosols are at low altitudes (1.5 km or less), the contribution from absorption is masked by the relatively more dominant Rayleigh scattering, resulting in negative values of AI. Theoretically, the aerosol index has a nearly linear relationship to AOT (for AOT₃₈₀ less than about 2) if the aerosols have a constant altitude and single scattering albedo [Torres *et al.*, 1998, Hsu *et al.*, 1999]. Hsu *et al.* [1999] showed that the EP-TOMS AI measurements were linearly proportional to the AOT₃₈₀ derived independently from AERONET Sun-photometer measurements over regions of biomass burning at Mongu and Zambezi, Zambia, between July and October of 1996 and 1997. However, their relationship cannot be directly compared in our study because of changes in the definition of the TOMS Aerosol Index in the most recent version 8 of their algorithm [O. Torres, personal communication], resulting in higher AI values for a given AOT. For this reason, we determined a new relationship between AI and AOT₃₈₀ retrievals from AERONET made within one hour of the EP-TOMS overpass time at the study sites dominated by smoke in southern Africa (i.e., Etosha Pan, Mongu, Ndola, and Senanga) during September 2000. Here we found $AI = 0.83 \times AOT_{380} - 0.4$, with $R = 0.66$.

In Figure 19 we scattered the monthly mean AI against the simulated monthly mean AOT₃₈₀. Here we restricted the geographic domain to a region dominated by biomass burning aerosols (i.e., 5°S to 20°S and 10°W to 35°E) and then separated the comparison by land (left column) and ocean (right column) points. The monthly mean AI was constructed using the Level

2 Aerosol Index product and same sampling method used to construct the monthly mean EP-TOMS AOT values. Here the model AOT₃₈₀ was sampled near the satellite overpass time, and only where the satellite daily grid box averages passed the pixel threshold test. The correlation coefficient (R), the number of locations (listed in parentheses), and equation of the line of best fit are reported in each scatterplot. In general, we find that our model results are linearly correlated to the aerosol index, with stronger correlations over the ocean. The model's regression line over land is not similar to that observed in the AERONET AOT₃₈₀ and EP-TOMS AI comparison discussed above (dashed line in Figure 19). The disagreement in the regression lines may be due to the model underestimating the AOT. As indicated above, when AERONET retrievals are greater than 1.0, the model underestimates the AOT by up to a factor of 2. The disagreement may also be due to the influence of other aerosol constituents that we are not simulating. Additionally, we find that EP-TOMS shows a larger AI over the ocean than over the land. Knowing that our simulations show smoke plumes rising in altitude as they move off the coast of Africa and that EP-TOMS observations are most sensitive to aerosols that are well above the surface, we would expect to see a larger signal by EP-TOMS off the coast, even though the column AOT may be greatest over the continent. The strong signal over the ocean may also be a result of sub-pixel cloud contamination (discussed above) or the age of the smoke aerosols where the condensation of trace gases cause the aerosols to become more absorbing.

3.1.5 Comparisons to Airborne and Ground-Based Measurements of Particle Size Distributions

In this section, we compare our simulated particle size distributions to AERONET retrievals and Passive Cavity Aerosol Spectrometer Probe 100X (PCASP) measurements. The AERONET column-integrated aerosol volume size distributions are obtained from the Level 2

AERONET product which uses the application of the *Dubovik and King* [2000] algorithm to spectral almucantar sky radiances and spectral AOT from the CIMEL Sun-sky radiometers. The PCASP instrument was onboard the C-130 of the UK Met Office airplane which flew within smoke source regions at altitudes between 208 m and 1000 m above ground level (AGL) during the SAFARI 2000 field campaign [*Haywood et al.*, 2003].

Figure 20 compares the daily mean simulated (solid line) and AERONET (dashed line) column-integrated volume size distributions at Etosha Pan on 13 September 2000. The model size distribution is normalized to the fine mode volume concentration of the AERONET retrieval. Compared to AERONET, we find that the model's fine mode is broader and has a larger fine mode median radius. Additionally, the simulated volume distribution of particles with radius sizes greater than 2 μm is up to a factor of 5 lower than AERONET. Knowing that Etosha Pan is influenced by sea salt and dust aerosols, which are large particles, the high coarse mode volume concentrations retrieved by AERONET may be a result of these aerosols. Since we are not simulating these aerosol sources, the model results will not be able to capture the high volume in the coarse mode. On the other hand, the base model is initialized with much higher volumes of coarse mode particles (Figure 2 – solid black line). This suggests that the model is either removing too many large particles or we are making incorrect assumptions about the smoke particle properties (i.e., density and shape), which is subsequently removing large particles too quickly. Further investigation of this issue is discussed in section 3.2.

Figure 21 compares the daily mean volume size distribution simulated by the base model (solid line) to the volume size distribution fitted to parameters reported by *Haywood et al.* [2003] which are representative of average PCASP measurements made in aged smoke plumes between 208 m and 294 m AGL (dashed line) at Etosha Pan on 13 September 2000. The model size

distribution is normalized to the fine mode volume concentration of the PCASP measurement. Again, we find that the model's fine mode is broader and has more larger-sized fine mode particles than the PCASP measurement. However, the volume of particles with radius sizes greater than 1 μm is approximately a factor of 3 greater than PCASP, and the peak of the coarse mode simulated by the base model is shifted towards larger particles. Since the PCASP instrument was flown through relatively young smoke aerosols, the measurement may show larger volumes of particles at smaller radius sizes than the model. On the other hand, since the model was initialized with a particle size distribution representative of young and aged smoke, by this time the size distribution has had time to grow and coagulate resulting in larger volumes of particles at larger fine mode radius sizes relative to PCASP. Seeing that the model overestimates the coarse mode particle mass relative to the elevated altitude PCASP measurements but underestimates the coarse mode mass relative to the column-integrated AERONET retrieval suggests that the coarse mode particles observed exist primarily near the surface and may not be transported over long distances.

3.2 Results – Sensitivity Tests

A series of sensitivity tests were conducted to understand the influence of various assumptions made in our model on the generality of our results. We partition these tests into two basic divisions. First, we consider a series of tests exploring the sensitivity of the model aerosol source to the timing and injection altitude of smoke emissions (Section 3.2.1). Second, we consider a series of tests exploring the sensitivity of the modeled aerosol properties to various assumptions about the particle microphysics, including initial particle size distribution, aging,

removal, and particle optics (Section 3.2.2). Each test is assigned a name, and a summary of the names and variances in each test are presented in Table 5.

3.2.1 Sensitivity of Simulated Aerosol Distributions to Timing and Injection of Emissions

In this section, we investigate how implementing a fluctuating daily emissions dataset, different aerosol emission injection altitudes, and diurnal cycle influences the model results.

3.2.1.1 Sensitivity to Daily versus Monthly Aerosol Emissions

An issue with using the GFED dataset is that it only provides monthly mean carbon emissions. An emission inventory with a finer temporal resolution may be important for realistically specifying the temporally varying simulated smoke optical properties. Therefore, rather than constantly emitting the same amount of aerosols throughout the month, we generated aerosol emissions that fluctuated day-by-day. The fluctuating daily aerosol emissions were constructed by correlating the emissions provided by the GFED to the Along Track Scanning Radiometer (ATSR) daily hot spot data. ATSR is a low-resolution sensor onboard the European Remote Sensing (ERS-2) satellite launched in April 1995 and has been used for fire location identification and environmental monitoring at visible and infrared wavelengths [Arino, 1995]. Here, we aggregated the daily ATSR hot spots to the same grid used in our model and emission source. The daily emissions for each grid cell are found by multiplying the monthly total emissions from the grid cell by the fraction of the monthly total fires occurring in the grid cell on that day. Potentially this underestimates the number of days on which our fires are active because heavy cloud or aerosol cover may mask fire hot spots that would otherwise be identified. On the other hand, the coarseness of the model grid might obviate this problem so that in an

average sense the day-to-day variability of fires occurring in the grid cell is about right. We note that the monthly mean emissions provided by the GFED dataset were constructed using the TRMM firecounts. However, we cannot use the TRMM firecounts here because of its irregular repeat cycle over a given region, which would cause it to sometimes miss a day entirely. In the monthly average sense, TRMM may be more useful because it sees more of the diurnal variability in emissions. We also note that we cannot use MODIS firecounts in this test because of problems with the MODIS detectors associated with hotspot detection during this time period [http://modland.nascom.nasa.gov/cgi-bin/QA_WWW/qaFlagPage.cgi?sat=terra].

In Figure 4 we compare the AOT_{500} simulated in this daily emissions case (referred to as Daily Emissions and represented by the dashed line) to our base model and AERONET measurements. This comparison shows that fluctuating the aerosol emissions through the month does have some impact on the day-to-day variability of the aerosol load, particularly at Mongu, Ndola, and Skukuza. However in some cases, the AOT_{500} comparison in our Daily Emissions test is worse, suggesting that simply using hot spots to scale the gridded GFED emissions may miss important variables that determine the actual day-to-day emissions, such as the size of the fire, the vegetation burned, or the diurnal cycle of emissions. Furthermore, this case cannot be used to explain the missing aerosol in the model in mid-September at Mongu or Senanga, suggesting that there is either a missing source in the GFED or the model meteorology is somehow incorrect in this region at this time. Still, the Daily Emissions case and the base case are more similar than they are different, suggesting that the variation in the numbers of fires and timing of the fires throughout the month are not as important as the variability in the meteorological conditions for the local AOT_{500} .

3.2.1.2 Sensitivity to the Diurnal Cycle of Aerosol Emissions

As pointed out earlier, *Eck et al.* [2003] reported a diurnal variability in AOT retrieved by AERONET at several sites during SAFARI 2000. This may be a result of real diurnal patterns in the fires themselves, in which case the observations are seeing the plumes from nearby sources, or the diurnal variability may reflect the aerosol morphology or venting from the planetary boundary layer. In our base model where the particles were injected between 0600 UTC and 1800 UTC every day, we found a very weak diurnal cycle in the simulated AOT at individual AERONET sites. Since we did not observe a strong diurnal trend in our base model, we conducted two additional tests where we varied the timing of emissions throughout the day. In one sensitivity test, we relaxed the base case diurnal cycle (referred to as “No DC” or no diurnal cycle) by evenly distributing the aerosol emissions throughout the day. In another test, we injected all the aerosols at the 1500 UTC timestep on each day (referred to as “1500 UTC”). Relative to the base case, changing the diurnal cycle of the aerosol emissions only had a small effect on the model extinction profile at the lowest altitudes (between 0 and 0.5 km) and almost no effect above that (not shown). In the test where nocturnal emissions were allowed, this suggests that those emissions can stay near the surface at night, but are quickly mixed throughout the boundary layer during the day. Overall, we are unable to reproduce the diurnal variability in AOT observed by *Eck et al.* [2003]. It is not clear that changes in aerosol morphology through any diurnal variations in the optics are to blame, as our computed aerosol optical properties agree reasonably well with the observations available (see Section 3.2.5). Therefore, it seems more likely that at the coarse spatial resolution of our model and the smoke emissions from point sources that AERONET is sensitive to are dispersed quickly in our grid.

3.2.1.3 Sensitivity to Aerosol Injection Height

To test the model's sensitivity to the altitude at which the aerosols are initially distributed vertically above their source regions, we ran two additional simulations that were based on information provided from the literature. During SAFARI 2000, trace gases and aerosols over the subcontinent were consistently observed as trapped stable layers at approximately 850 hPa (~1.5 km), 700 hPa (~3.0 km), and 500 hPa (~5.5 km) within the lower troposphere [Stein *et al.*, 2003, Schmid *et al.*, 2003, McGill *et al.*, 2003]. The injection altitude of aerosol emissions was assumed to be associated with buoyancy generated by the release of heat in the fires, and the amount of heat release was found to be dependent on the amount and type of vegetation being burned, and whether the combustion was smoldering or flaming [Andreae and Merlet, 2001]. Using this information, we ran one simulation with aerosol emissions centered at three model layers and referred to as the 3-Layers model (Layers included: 1.42 km (0.41 km thick), 3.06 km (0.67 km thick), and 5.64 km (0.98 km thick)). In another simulation, we emitted the aerosols within one model layer, centered at 2.42 km (0.58 km thick) and this test is referred to as the 2 km-Layer model.

Figures 10 and 11 show mean vertical extinction profiles for the test simulations. For a one-day comparison (Figure 10), we find that the overall vertical profiles of the aerosol are almost uniform with altitude. The results from the 2 km-Layer model is not shown in Figure 10 since the results are nearly identical to the base model. However in the 3-Layers model, the aerosols get carried downwind more rapidly due to the higher wind speeds aloft, thereby producing extinction values that are too low relative to the observations and base model. In Figure 11, we compare the tests to the monthly mean MPLNET lidar observations at Skukuza. Here a different picture emerges where we find that the simulated vertical profiles from our two

elevated injection tests are not similar to the base model. Instead, the aerosol appears to reside at an elevated altitude relative to both the base case and the observations. Our base model of uniform mixing throughout the depth of the PBL is therefore the most comparable to the observations.

3.2.2 Sensitivity of Simulated Aerosol Properties to Microphysical Processes

In this section we discuss the implications and limitations of various assumptions made about the aerosol microphysics in our model, including choices of initial particle size distribution, resolution of bin sizes, optical properties, and aerosol aging and removal processes.

3.2.2.1 Sensitivity to Treatment of Particle Size Distribution

CARMA is a bin-resolving cloud and aerosol microphysics module. Incorporation of such a module into a large-scale transport-modeling framework can easily become computationally prohibitive. To reduce this computational expense, CARMA can be adjusted to use the fewest number of size bins and microphysical processes necessary to carry out a given problem. In contrast, a more typical chemical transport model undertaking the problem we presented here might have a greatly reduced aerosol microphysical modeling capability compared to CARMA. As an example, the NASA Global Ozone Chemistry Aerosol Radiation and Transport (GOCART) model [Chin *et al.* 2002] neglects the explicit treatment of aerosol particle size distributions for carbonaceous particles, instead partitions the aerosols into hydrophobic and hydrophilic organic carbon (OC) and black carbon (BC) components. The subdivision of the aerosol mass to hydrophilic and hydrophobic components affects the aerosol optics, as well as the aerosol lifetime since only the hydrophilic fraction is scavenged by

precipitation. The time-scale for conversion of hydrophobic to hydrophilic aerosols in these models is typically short (approximately 1 day) and is intended to represent condensation of gases and water absorption onto the particles, but does not allow for explicit treatment of other aging mechanisms such as coagulation or the treatment of the aerosol optics as internal mixtures. On the other hand, it should be pointed out that GOCART is more complete than our model in the sense that it treats all major tropospheric aerosols species.

The principle strength of our model is the explicit treatment of specific microphysical aging processes through coagulation and sedimentation, which is a step towards evolving internally mixed aerosol species. A question we present here is how many size bins are required to adequately constrain our problem. Based on earlier simulations (e.g., Colarco *et al.* [2004]), we chose to use 16 size bins spaced from 0.01 – 10 μm radius in our base model. As a limiting case, we also considered a case with 22 size bins spaced between 0.05 – 15 μm radius which is identical to the bin separation AERONET uses to report their size distributions. Using the refractive index and particle size distribution retrieved on 16 September 2000 at Ndola, we compute the Ångström exponent for the 440 and 870 nm wavelength pair ($\alpha_{440/870}$) and curvature term at 380, 500, and 870 nm wavelengths ($\alpha'_{380/500/870}$) for the 16-bin and 22-bin cases, and then compared the values to the AERONET observation on this particular day. Here, we find that the $\alpha_{440/870}$ is 1.93, 1.97, and 1.96, respectively, for the AERONET observation, 16-bin case, and 22-bin case. Additionally, the curvature terms are 1.21, 1.03, and 1.12, respectively, for the same three cases. Here, the computed Ångström exponents are similar to the observed value, and presumably the differences can mainly be attributed to actual particle non-sphericity reflected in the measured values. On the other hand, compared to the observations, the computed curvature terms are approximately 20% and 10% smaller in the 16-bin case and 22-bin case, respectively.

Note that the curvature term was defined in terms of the 380, 500, and 870 nm wavelengths, and of those three wavelengths AERONET only retrieves refractive indices at 870 nm. Here, we interpolate the 500 nm refractive index from the 440 and 670 nm retrieved values. Additionally, the 380 nm refractive index is assumed to be the same as the 440 nm retrieved value, which seems to be a reasonable assumption based on the discussion in *Torres et al.* [2005]. The results of our calculations are essentially the same when we employ the wavelength independent refractive index used in our previous base model calculations.

The discrepancy in the computed curvature terms above can be attributed to the number of size bins used to resolve the fine mode portion of the particle size distribution. We note that there is essentially no contribution to either the Ångström exponent or curvature term from particles smaller than 0.05 μm radius or larger than 10 μm radius. The fine mode particle scattering area is primarily between particles 0.05 and 0.6 μm radius, which comprises six size bins in our 16-bin case and nine size bins in our 22-bin case. From sensitivity tests with more bins (not shown), we find that increasing the number of size bins in the fine mode improves the accuracy of the computed optics. Here we find a convergence in the accuracy of the computed optical properties when ten or more bins are used in the fine mode particle size distribution (i.e., between 0.05 and 0.7 μm). The improved accuracy of the optics by adding more size bins is also illustrated in the comparison of the initial particle size distribution simulated Ångström exponent for the 380 and 440 nm wavelength pair, which is 1.48, 1.52, and 1.47 for the observation, 16-bin case, and 22-bin case, respectively. The discussion above focuses on the uncertainty in the prescribed initial particle size distribution used in the model, and the model's ability to reproduce the observed optical properties. In the following discussion, we consider different assumptions about the initial particle size distribution and how that evolves in the model.

Our simplest sensitivity test is called the Mass model. Here we simply integrate the mass across all the size bins in our base model and compute the aerosol optical properties following *Chin et al.* [2002], assuming the aerosols were completely hydrophilic because of the short timescale for conversion. We also consider different assumptions about the initial particle size distribution based on retrievals by AERONET (column-integrated) or measurements made by the airborne PCASP instrument (*in situ*) [Haywood *et al.*, 2003] over smoke source regions during the SAFARI 2000 field campaign. In the PCASP model we used a particle size distribution that was a fit to parameters determined from mean PCASP observations taken within a smoke plume at Otavi, Namibia on 13 September 2000. The AERONET-Mean model used a particle size distribution that was fitted to the mean parameters of smoke dominated days retrieved at Ndola, Zambia by AERONET in September 2000. The 22-Bins model resolves the particle size distribution using the AERONET reported bins as described above. Table 5 lists the model names, input parameters that were changed in each model, and the number fractions, geometric standard deviations and median number radii associated with each particle size distribution. Figure 2 presents the column-integrated volume size distributions that were implemented into the models.

Table 2 lists the monthly mean AOT_{500} , $\alpha_{380/440}$, α' , SSA_{440} , SSA_{670} , SSA_{870} , and SSA_{1020} of smoke dominated days for selected sensitivity tests at Ndola and Inhaca. Note that not all of the results are shown for Inhaca since they show the same conclusions as at Ndola. In general, we find that the simulated mean AOT_{500} and SSA are the most sensitive to Mass and PCASP parameterizations. Compared to the base model, the Mass model mean AOT_{500} is approximately 50% higher at both study sites. The reason for this is that the Mass model implicitly assumes that all the aerosol mass is in the fine mode, which has greater aerosol extinction per unit mass than

the coarse mode. However, the low monthly mean Ångström exponent ($\alpha = 1.27$) of the Mass model at both locations suggests that its assumed fine mode particle size distribution has a slightly larger median radius than the base model or observations. We also find that the Mass model is approximately 55% more absorbing than the base model at both study sites.

We also find that the PCASP model monthly mean AOT_{500} is approximately 28% lower than the base model at Ndola. The high mean Ångström exponent ($\alpha = 1.66$) of the PCASP model suggests that this model is transporting more smaller sized particles relative to the base model, but the lower mean curvature value suggests a greater relative contribution of coarse mode particles to the total AOT. Figure 22 compares the simulated column-integrated volume size distributions of the base and PCASP models to the AERONET retrieval on 16 September 2000 at Ndola. The model size distributions are normalized to the fine mode volume concentration retrieved by AERONET. Here we find that the PCASP model has a smaller fine mode median radius compared to base model, but a larger volume (mass) concentration at radius sizes between 1.0 and 10 μm , which explains the higher Ångström exponent (smaller fine mode) but lower optical depth and curvature term (more of the mass in the coarse mode). We also find that the PCASP model is roughly 25% more absorbing than the base model at both study sites.

The monthly mean AOT_{500} , curvature term and SSA results from the AERONET-Mean model were not significantly different from the base model results at Ndola (see Table 2). However, the mean Ångström exponent [380/440] of the AERONET-Mean model is higher than the base model suggesting that the AERONET-Mean model has a smaller fine mode median radius.

As discussed above, we find that the 22-Bins model does impact our computed optical properties. Here we find that the monthly mean $\alpha_{380/440}$ is slightly lower and the curvature value

is higher than the base model which has 16 size bins. These results are consistent with our findings of the initial calculations of the 16-bin case and 22-Bin case discussed above. We also find that the 22-Bins model monthly mean $\alpha_{380/440}$ and curvature values differ from the AERONET observations. By increasing the bin resolution of the model, we are able to observe more details about the simulated particle size distribution than illustrated in the base model alone. Here, the $\alpha_{380/440}$ of the 22-Bins model and AERONET observation is 1.32 and 1.43, respectively, which suggests that the particle fine mode median radius is too large in the model relative to the observations. The curvature term of the 22-Bins model and AERONET observation is 1.38 and 1.23, respectively, suggesting that relative to AERONET too much of the aerosol optical thickness is due to the fine mode. This point is qualitatively born out in almost all of our simulations because the model does not maintain the observed concentration of coarse mode particles (see Figure 22 for the 16-bin base case and discussion in Section 3.2.2.3). To explain the lower Ångström exponent we recall that the initial particle size distribution already included some effects of aging and coagulation of smoke particles so that further coagulation has made the fine mode median radius slightly too large.

Overall, these results suggest that the transport of a size distribution and the appropriate bin resolution of the accumulation mode in our model are important in order to obtain optical properties that are comparable to AERONET. The Mass model produced mean AOT₅₀₀ values that were higher and aerosols that were more absorbing than both the base model and AERONET at the study sites. Additionally, the Mass model has the disadvantage that it cannot capture the aging of the particles as they evolve over several days. *Westphal et al.* [1991] and *Colarco et al.* [2004] simulated the evolution of smoke clouds over several days and found that the aerosol optical properties changed as the particles evolved by coagulation. *Westphal et al.*

[1991] demonstrated that small changes in the geometric mean radius yielded large changes in extinction and absorption efficiencies and therefore in the specific extinction and absorption. However, the sign of the change depended on the size distribution. *Eck et al.* [1999] found that the mode size was positively correlated with the aerosol optical thickness. *Reid et al.* [1998] suggested that this increase in radius was due to the aging processes of smoke aerosols, whereby the particle size increases with time because of both coagulation and gas-to-particle conversion. Our model does not include gas to particle conversion, but the impact of coagulation is discussed below.

3.2.2.2 Sensitivity to Microphysical Processes

The size of the aerosol is important when calculating optical properties because different particle sizes scatter different amounts of radiation. Several observational studies have shown that aerosol size distributions shift from fine mode particle sizes to accumulation mode particle sizes as the aerosol ages due to both coagulation and gas-to-particle conversion [*Reid and Hobbs*, 1998; *Reid et al.*, 1998; *Eck et al.*, 2001; *Eck et al.*, 2003; *Haywood et al.*, 2003]. Simulations of smoke aerosols over multi-day periods have also suggested that coagulation is necessary in order to explain the change in particle size distributions and optical properties as the smoke ages [*Westphal et al.*, 1991; *Colarco et al.*, 2004]. In this section, we investigate the model's sensitivity to coagulation by conducting a simulation where the particles were not allowed to coagulate (referred to as the No Coagulation model).

In our No Coagulation simulation, we find that the mean AOT_{500} of smoke dominated days is approximately 10% lower than the base model at Ndola. Additionally, the Ångström exponent is higher while the curvature term is lower relative to both the base model and the

AERONET observations (Table 2). The computed SSA for the No Coagulation model was slightly lower (i.e., more absorbing) than both the base model and the AERONET observation, although both the base and No Coagulation models are within the uncertainty of the AERONET retrieval error bars. The interpretation of these results is rather complicated by the uncertainty in the resolution of the spectral optical properties in our base model. At first glance, the higher Ångström exponent and lower curvature values of the No Coagulation model suggest too small of a fine mode median radius and excessive contribution from coarse mode particles to the total AOT. However, initializing our model with a particle size distribution that already includes some aged aerosols and then allowing the particles to coagulate further exaggerates the effects of coagulation making it difficult to reproduce the correct optical properties. Therefore, the No Coagulation model where we already implicitly include coagulation may be a more reasonable approximation for the aerosol optical properties over southern Africa. Here the base model is probably more reasonable for long-range transport of the aerosols over longer periods of time, which is consistent with *Westphal et al.* [1991] and *Colarco et al.* [2004].

3.2.2.3 Sensitivity to Removal Schemes

The properties of smoke particles vary depending on fuel type and moisture, combustion phase, and wind conditions. These properties can also change rapidly as they disperse. In general, smoke particles are composed of ~60% organic carbon and ~5-10% black carbon, 80-90% of their volume is in the accumulation mode, reported density varies between 0.79 and 1.35 g cm⁻³, and studies have shown smoke particles to have a variety of morphologies such as chain aggregates, solid irregulars, and more liquid/spherical shapes [*Reid et al.*, 2004]. About ~10% of the smoke volume consists of a variety of coarse mode particles (~2.5-15 µm). These coarse

mode ash particles ($2 < d_p < 20 \mu\text{m}$) have been observed more than fifty kilometers from the source [Reid *et al.*, 2004]. However, the density and exact shape of these giant ash particles is unknown to our knowledge.

Since the model's volume concentrations of particles greater than $2 \mu\text{m}$ were found to be approximately a factor of 5 too low, this suggests that we are most likely not treating the large particles correctly in our model. There are two possibilities that may explain this model error. First, given the large uncertainty in the coarse mode of the AERONET size distribution retrievals, we may not be representing the coarse mode particles properly in our model. Second, our removal processes (i.e., dry deposition routine) may not be appropriate for this region. Currently, we are treating all of the smoke particles by applying the same particle density (1.35 g cm^{-3}) and spherical shape to all the particle sizes. However the coarse mode particles could consist of ash particles, which could have low density and irregular shape. For these reasons, we conducted two additional simulations; one in which we changed the particle density to 0.675 g cm^{-3} (i.e., half the base model density and referred to as Density model) and another in which we made the particles flat-plates by following Fuchs [1964] (referred to as Shape model). On the other hand, we may be using the appropriate smoke properties in our base model, however the dry deposition parameterization used to calculate the dry deposition velocities may be removing the large particles in our model too vigorously. Therefore, we conducted two additional simulations; one where we did not allow the particles to be removed via dry deposition (referred to as No Dry Dep. model) and another where we implemented an alternative method to calculate the dry deposition velocities (referred to as Zhang *et al.* [2001] model). The alternative dry deposition calculation we examined in this study follows the parameterization described by

1023 *Zhang et al.* [2001] which is more robust than the current dry deposition routine by *Shao* [2000].
1024 In particular, the *Zhang et al.* [2001] considers surface type where *Shao* [2000] does not.

1025 Figure 23 shows the normalized daily mean column-integrated volume size distribution
1026 retrieved by AERONET and simulated by the test models at Ndola, Zambia on 16 September
1027 2000. The model distributions are normalized to the fine volume concentration retrieved by
1028 AERONET. For clarity, we did not present the results from the Shape or *Zhang et al.* [2001]
1029 models since the fine mode results were similar to the base model and the coarse mode results
1030 were similar to the Density model. In general, we find that different particle shapes and densities,
1031 and an alternative method in computing the dry deposition velocities improve the volume of the
1032 coarse mode particles but not enough to be comparable to the AERONET retrievals. The
1033 combination of all three modifications (density, shape, and dry deposition method) in a single
1034 simulation provided results that were the most comparable to AERONET (not shown but similar
1035 to the Density fine mode and the No Dry Dep. coarse mode). Of the results shown in Figure 23,
1036 the only method that reproduced similar volume concentrations of particles greater than 2 μm
1037 relative to AERONET was the No Dry Dep. model. Since we are able to maintain the large
1038 particles in the No Dry Dep. model, this suggests that our model has problems transporting large
1039 particles. On the other hand, since the initial particle size distribution in the model may represent
1040 both local and transported aerosols, the coarse mode of the transported aerosol may have been
1041 even more pronounced at the source. Thus, our base case may not be initialized with enough
1042 coarse mode particles. Altogether, without more information about the properties of the coarse
1043 mode smoke particles, in particular about the ash particles, we do not know which method is the
1044 most appropriate to use in our model. Further investigation of the smoke size distribution is
1045 subject of future research.

Of the tests conducted in this section, we found that the simulated optical properties were significantly impacted by the change in particle density. Since we want to maintain the same injected total particle mass, decreasing the particle density by half doubles the number of particles injected which results in increasing both the rate of coagulation of fine mode particles and the computed AOT, but decreasing the computed Ångström exponent. The optical properties of the other tests in this section are essentially the same as the base model. The slightly lower curvature terms of these tests relative to the base model are expected and due to the additional coarse mode particles each test provides.

3.2.2.4 Sensitivity to Smoke Optics

In this section, we investigate how the choice of refractive index and relative humidity influences the model results.

To examine the model's sensitivity to choice of refractive index, we tested four different refractive indices that are representative of biomass burning aerosols (Table 5). The refractive indices tested here were either calculated by *Haywood et al.* [2003] or retrieved by AERONET. *Haywood et al.* [2003] calculated a refractive index of $1.54 - 0.025i$ at 550 nm for young smoke aerosols. This refractive index was applied to all wavelengths (wavelength independent (WI)) and referred to as the WI-Haywood et al. [2003] model. We also selected a refractive index retrieved on 16 September 2000 at Ndola by AERONET ($N_{\text{ref}} = 1.52 - 0.019i$ at 500 nm). Again, we chose this particular day since it had the highest AOT_{500} which suggests that this day was largely dominated by smoke aerosols. This refractive index was applied to all wavelengths and referred to as the WI-AERONET model. We also explored wavelength dependent (WD) refractive indices, which are listed in Table 5. The WD-AERONET model applied refractive

indices retrieved by AERONET on 16 September, and the WD-AERONET-Mean model applied the mean refractive indices of smoke dominated days retrieved by AERONET at Ndola, Zambia.

Here we find that the monthly mean AOT_{500} and Ångström exponent [380/440] of smoke dominated days are not significantly sensitive to the choice of complex refractive index (Table 2). However, we did find that the simulated mean curvature values and SSA were sensitive to our choice of refractive index (see Table 2 and Figure 24). Compared to the base model, the WI models have higher curvature values, while the WD models have lower curvature values. Additionally, all but the WI – Haywood et al. [2003] model have higher mean SSA (i.e., more absorbing aerosols) than the base model. Overall, we find that the WI refractive indices are the most comparable to the AERONET observations where the WD cases are not.

To test the model's sensitivity to relative humidity, we considered a test where we assumed that the relative humidity at all locations was zero (referred to as No RH model). Compared to the base model, we find that when we do not treat the humidification of aerosols, the mean AOT_{500} is lower and the particles become more absorbing at Ndola. However, the Ångström exponent and curvature terms remain relatively unchanged (Table 2).

Overall, we find that WI refractive indices and treating relative humidity produces optical properties that are the most comparable to AERONET observations at Ndola.

4. Conclusions

In this study, we investigated the transport and optical properties of biomass burning aerosols using a three-dimensional aerosol microphysical, transport, and radiation model. Our first goal in this study was to determine if using estimated aerosol emissions, measured particle size distributions, and estimated injection altitudes collected during the SAFARI 2000 field

campaign as input parameters in our model allowed us to reproduce the observed optical properties. Our second goal was to better understand the microphysics needed to accurately simulate biomass burning aerosol properties over our domain. The principle findings of our study are summarized as follows:

1. *Comparisons to AERONET AOT:* We find that our base model, which uses a satellite-derived monthly inventory of biomass burning emissions and AERONET derived aerosol optical properties, was sufficient to reproduce the majority of the day-to-day variability in AOT at the six AERONET sites used in this study. In certain instances where the model significantly underestimated the aerosol loading with respect to AERONET, we found from satellite imagery that the model had misplaced the smoke plume relative to observations, suggesting errors in the model dynamics. Sensitivity tests in which we varied the diurnal emissions of the smoke or the timing of emissions throughout the month using daily satellite firecounts showed little effect on the daily variability of simulated AOT at the selected AERONET locations. Although these results do not exclude possible errors in the biomass burning emission inventory used, they suggest that the aerosol loading over the continent is most strongly controlled by dynamics, which is consistent with results from *Myhre et al.* [2003]. On a monthly basis, the model reproduces mean AOT values which are lower than those observed at the six AERONET sites, suggesting either an uncertainty in the magnitude of our aerosol emissions or that we are neglecting contributions from other aerosol species.

2. *Comparisons to Satellite Observations of AOT*: Comparisons of the model AOT to satellite observations showed that our model is capable of simulating smoke plume features similar to those observed by SeaWiFS, MODIS, MISR, and EP-TOMS over southern Africa and the Atlantic Ocean. Qualitatively, this suggests that the input parameters and microphysical processes in our model are adequate for this study region. In order to quantitatively compare our model to the satellite observations we constructed monthly mean regional AOT maps in which the model observations were weighted and sampled in manner consistent with the available satellite observations. We find that the simulated monthly mean AOT is linearly correlated to the satellite observations over the land and ocean, but that the model is consistently lower than the satellite observations. Over land, we find that our model results compare best to MISR with the strongest correlations and slope nearest to 1. At the AERONET sites, the model compares best to MISR at the four sites dominated by biomass burning, while the model compares best to MODIS at the two remaining sites which are influenced by multiple aerosol sources. Over the ocean, the model compares the best to MODIS. Over both land and ocean we find the largest disagreements between the model and EP-TOMS. These results may reflect the differences in the retrieval technique of each satellite. Here the MISR algorithms may be more appropriate for retrievals dominated by a single aerosol source, while the MODIS algorithms may be more appropriate for retrievals with multiple aerosol sources. Due to the large pixel size of the EP-TOMS retrievals, the large disagreement between the model and EP-TOMS may be a result of sub-pixel clouds that are not being removed from their retrievals. While sub-pixel cloud contamination may affect all the aerosol retrievals,

1137 this might be expected to be the most pronounced over the ocean where we find
1138 generally fewer pixels available for constructing our monthly means than over land.
1139 The disagreement among the model and satellite observations may also be due to the
1140 contributions of other aerosol species to the column AOT, which might be more
1141 pronounced over the ocean than land. Additionally, we cannot exclude the errors in
1142 the assumptions of the aerosol optical properties used in the satellite retrievals or in
1143 the model. In particular, MODIS uses a different retrieval algorithm over land points
1144 than over the ocean. Overall, the consistently lower AOT simulated by the model
1145 relative to MODIS and MISR over the ocean, and the good agreement between
1146 MODIS and MISR over the ocean suggests that the model is missing important
1147 aerosols or processes. However, the disagreement between MODIS and MISR over
1148 the land does not provide us with enough information to determine the model's
1149 performance over continental Africa.

- 1150
- 1151 3. *Comparisons to Airborne and Ground-Based Measurements of Extinction:* The
1152 simulated vertical extinction profiles from our base model compare favorably to the
1153 AATS-14, MPL, and CPL measurements. The minor differences found between the
1154 simulations and observations on a single day may be a result of the model's coarse
1155 resolution and source function. Given that our source function cannot represent the
1156 likely variations in daily smoke emissions, it is challenging to reproduce individual
1157 days. However, the model's vertical resolution is sufficient in representing long time-
1158 scale averaged vertical profiles. When exploring simulations with elevated aerosol

injections, we found that our best results were with our base model assumption of injections uniformly mixed within the planetary boundary layer.

4. *Comparisons to Measurements and Retrievals of Particle Microphysical and Optical*

Properties: While the base model compares favorably to daily and monthly observations of AOT by AERONET, it does not capture the daily variability in the Ångström exponent and retrieved single scatter albedo. It is likely that the model remains consistent because of its relatively invariant aerosol composition. At the selected sites, the observed fluctuations may be due to the diurnally varying contributions from dust and other aerosol species that are not simulated in this study. On a monthly mean basis, the modeled spectral dependence of the AOT and single scatter albedo compare favorably with the AERONET observations at Ndola (and the other smoke dominated sites) and slightly less at Inhaca (which has important contributions from non-smoke aerosols). Comparisons of the simulated particle size distribution to AERONET retrievals and airborne PCASP measurements reveal that the model base case evolves a slightly larger fine mode median radius than both sets of observations. Additionally, these particle size distribution comparisons show that the model overestimates the coarse mode particle mass relative to the elevated altitude PCASP measurements but underestimates the coarse mode mass relative to the AERONET retrieval. Assuming that there is no error in the AERONET volume distribution of the coarse mode, the latter point suggests that the coarse mode particles observed exist primarily near the surface and may not be transported over long distances. We also found that the model is evidently too aggressive in removing

these coarse mode particles, and sensitivity tests suggest that different assumptions about the composition, shape, or density of the coarse mode particles would help with this issue. On the other hand, the larger fine mode median radius in the base model may be due to our assumption about the initial particle size distribution, which already includes some effects of the smoke aging. These general points are further illustrated in the optical calculations presented in Table 2. The results of these tests indicate that the simulated optical properties are relatively insensitive to choices of particle refractive index or humidification (i.e., composition), but are sensitive to the choice of initial particle size distribution and, as discussed in Section 3.2.2.1, to the number of size bins used to resolve the fine mode fraction of the particle size distribution. Here we find that initializing the model with the airborne PCASP measured particle size distribution does not represent the evolution of the coarse mode, and the Mass model does not reproduce the observed optical properties. Initializing the model with the AERONET size distribution retrieved at Ndola leads to too large of a fine mode median radius relative to the observations. Overall, for a model that treats coagulation, the implication is that the fine mode needs to be initialized to a smaller median radius than what is reported by AERONET. Sensitivity tests of the optical calculations further suggest that at least ten size bins are needed to adequately resolve the optical properties of the evolving fine mode.

Since Africa experiences the most extensive biomass burning in the world, this work is a step toward improved quantification of smoke optical properties for use in calculating the direct effects of these aerosols on climate, and suggests methods for incorporating the particle size

1205 distribution of smoke aerosols into microphysical models attempting to simulate the aging of
1206 smoke particles. However, we did find inconsistencies in the AOT land comparisons among
1207 AERONET, MISR, MODIS, EP-TOMS data that need to be better understood in order for us to
1208 feel confident in using them to aid us in modeling and reducing the uncertainty in aerosol
1209 forcing. These inconsistencies and further investigation of aging mechanisms inspire further
1210 research.

1211 Acknowledgments

1212 This work was supported by NSF-ATM0435713 and NIP/03-0000-0043. Rebecca Matichuk was
1213 partially supported by the NASA Goddard GSRP program. We also thank the following people
1214 and groups for kindly providing data and assisting us with the satellite, aircraft, and ground-
1215 based data used in our study: B. N. Holben (AERONET data), R. Kahn (MISR data), R. Levy
1216 (MODIS data), O. Torres (EP-TOMS data), M. McGill and D. Hlavka (CPL), B. Schmidt
1217 (AATS-14 measurements), J. Spinhirne and NASA Earth Observatory System (MPL data), G.
1218 van der Werf (GFED data), S. Korontzi (Smoke Emissions), and L. Zhang (Dry Deposition
1219 Routine).

1220

1221 References

- 1222 Abdou, W. A., D. J. Diner, J. V. Martonchik, C. J. Bruegge, R. A. Kahn, B. J. Gaitley, K. A.
 1223 Crean, L. A. Remer, B. Holben, Comparison of coincident Multiangle Imaging
 1224 Spectroradiometer and Moderate Resolution Imaging Spectroradiometer aerosol optical
 1225 depths over land and ocean scenes containing Aerosol Robotic Network sites, *J. Geophys.*
 1226 *Res.*, 110, D10S07, doi:10.1029/2004JD004693, 2005.
- 1227 Ackerman, A, O Toon, P Hobbs, A model for particle microphysics, turbulent mixing, and
 1228 radiative-transfer in the stratocumulus-topped marine boundary-layer and comparisons with
 1229 measurements, *J. Atmos. Science*, 52(8), 1204-1236, 1995.
- 1230 Andreae, M. O., The influence of tropical biomass burning on climate and the atmospheric
 1231 environment, *Biogeochemistry of Global Change: Radiatively Active Trace Gases*,
 1232 Oremland, R. S. (ed.), Chapman & Hall, New York, NY, 113-150, 1993.
- 1233 Andreae, M. O., P. Merlet, Emission of trace gases and aerosols from biomass burning, *Global*
 1234 *Biogeochem. Cycles*, 15(4), 955-966, 10.1029/2000GB001382, 2001.
- 1235 Annegarn, H. J., L. Otter, R. Swap, and R. Scholes, Southern Africa's ecosystem in a test-tube-A
 1236 perspective on the Southern African Regional Science Initiative (SAFARI 2000), *S. Afr. J.*
 1237 *Sci.*, 98, 111-113, 2002.
- 1238 Arino, O., A. Buongiorno, P. Goryl, Intercalibration of AVHRR and ATSR data, *Calibration*
 1239 *and Applications of Satellite Sensors for Environmental Monitoring Advances in Space*
 1240 *Research*, 17(1), 29-38 1995.
- 1241 Barbosa, P. M., D. Stroppiana, J.-M. Grégoire, J. M. C. Pereira, An assessment of vegetation fire
 1242 in Africa (1981 - 1991): Burned areas, burned biomass, and atmospheric emissions, *Global*
 1243 *Biogeochem. Cycles*, 13(4), 933-950, 10.1029/1999GB900042, 1999.

1244 Barth, M. C., P. J. Rasch, J. T. Kiehl, C. M. Benkovitz, S. E. Schwartz, Sulfur chemistry in the
 1245 National Center for Atmospheric Research Community Climate Model: Description,
 1246 evaluation, features, and sensitivity to aqueous chemistry, *J. Geophys. Res.*, 105(D1), 1387-
 1247 1416, 10.1029/1999JD900773, 2000.

1248 Chin, M., P. Ginoux, S. Kinne, O. Torres, B. Holben, B. Duncan, R. Martin, J. Logan,
 1249 A. Higurashi and T. Nakajima, Tropospheric Aerosol Optical Thickness from the GOCART
 1250 Model and Comparisons with Satellite and Sun Photometer Measurements, 59(3), 461–483,
 1251 2002.

1252 Colarco, P. R., O. B. Toon, O. Torres, and P. J. Rasch, Determining the UV imaginary index of
 1253 refraction of Saharan dust particles from Total Ozone Mapping Spectrometer data using a
 1254 three-dimensional model of dust transport, *J. Geophys. Res.*, 107 (D16), 4312,
 1255 doi:10.1029/2001JD000903, 2002.

1256 Colarco, P. R., O. B. Toon, B. N. Holben, Saharan dust transport to the Caribbean during
 1257 PRIDE: 1. Influence of dust sources and removal mechanisms on the timing and magnitude
 1258 of downwind aerosol optical depth events from simulations of in situ and remote sensing
 1259 observations, *J. Geophys. Res.*, 108 (D19), 8589, doi:10.1029/2002JD002658, 2003a.

1260 Colarco, P. R., et al., Saharan dust transport to the Caribbean during PRIDE: 2. Transport,
 1261 vertical profiles, and deposition in simulations of in situ and remote sensing observations, *J.*
 1262 *Geophys. Res.*, 108 (D19), 8590, doi:10.1029/2002JD002659, 2003b.

1263 Colarco, P. R., M. R. Schoeberl, B. G. Doddridge, L. T. Marufu, O. Torres, E. J. Welton,
 1264 Transport of smoke from Canadian forest fires to the surface near Washington, D.C.:
 1265 Injection height, entrainment, and optical properties, *J. Geophys. Res.*, 109, D06203,
 1266 doi:10.1029/2003JD004248, 2004.

- 1267 Colella, P, and P Woodward, The numerical-simulation of two-dimensional fluid-flow with
1268 strong shocks, *J. Computational Physics*, 54(1), 115-173, 1984.
- 1269 Crutzen, O. J. and M. O. Andreae, Biomass burning in the tropics – Impact on atmospheric
1270 chemistry and biogeochemical cycles, *Science*, 250, 669-1678, 1990.
- 1271 Diner, DJ, Beckert JC, Reilly TH, Bruegge CJ, Conel JE, Kahn RA, Martonchik JV, Ackerman
1272 TP, Davies R, Gerstl SAW, Gordon HR, Muller JP, Myneni RB, Sellers PJ, Pinty B, and
1273 Verstraete MM, Multiangle imaging spectroradiometer (MISR) instrument description and
1274 experiment overview, *IEEE Trans. Geosci. Remote Sens.*, 36, 1072-1087, 1998.
- 1275 Dubovik, O., M. D. King, A flexible inversion algorithm for retrieval of aerosol optical
1276 properties from Sun and sky radiance measurements, *J. Geophys. Res.*, 105(D16), 20673-
1277 20696, 10.1029/2000JD900282, 2000.
- 1278 Dubovik, O., B. Holben, T. Eck, A. Smirnov, Y. Kaufman, M. King, D. Tanre, and I. Slutsker,
1279 Variability of absorption and optical properties of key aerosol types observed in worldwide
1280 locations, *J. Atmos. Sci.*, 59, 2002.
- 1281 Dwyer, E., J. M. Pereira, J. M. Gregorie, and C.C. DaCamara, Characterization of the spatio-
1282 temporal patterns of global fire activity using satellite imagery for the period April 1992 to
1283 March 1993, *J. of Biogeography*, 27(1), 57-69, 2000.
- 1284 Eck, T. F., B. N. Holben, J. S. Reid, O. Dubovik, A. Smirnov, N. T. O'Neill, I. Slutsker, S.
1285 Kinne, Wavelength dependence of the optical depth of biomass burning, urban, and desert
1286 dust aerosols, *J. Geophys. Res.*, 104(D24), 31333-31350, 10.1029/1999JD900923, 1999.
- 1287 Eck, T. F., B. N. Holben, D. E. Ward, O. Dubovik, J. S. Reid, A. Smirnov, M. M. Mukelabai, N.

1288 C. Hsu, N. T. O'Neill, I. Slutsker, Characterization of the optical properties of biomass
 1289 burning aerosols in Zambia during the 1997 ZIBBEE field campaign, *J. Geophys. Res.*,
 1290 106(D4), 3425-3448, 10.1029/2000JD900555, 2001.

1291 Eck, T. F., et al., Variability of biomass burning aerosol optical characteristics in southern Africa
 1292 during the SAFARI 2000 dry season campaign and a comparison of single scattering albedo
 1293 estimates from radiometric measurements, *J. Geophys. Res.*, 108 (D13), 8477,
 1294 doi:10.1029/2002JD002321, 2003.

1295 Fuch, N. A., The Mechanics of Aerosols, Dover Publications, INC., New York, 1964.

1296 Giglio, L., J. D. Kendall, and R. Mack, A multi-year active fire data set for the tropics derived
 1297 from the TRMM VIRS, *International Journal of Remote Sensing*, 24, 2003.

1298 Hao, W. M., M. H. Liu, P. J., Crutzen, Estimates of annual and regional releases of CO₂ and
 1299 their trace gases to the atmosphere from fires in the tropics, based on the FAO statistics for
 1300 the period 1975-1980, *Fire in the Tropical Biota: Ecosystem Processes and Global*
 1301 *Challenges, Ecol. Studies 84* (ed. Goldammer), pp. 440-462. Springer-Verlag, New York,
 1302 1990.

1303 Haywood, J. M., S. R. Osborne, P. N. Francis, A. Keil, P. Formenti, M. O. Andreae, and P. H.
 1304 Kaye, The mean physical and optical properties of regional haze dominated by biomass
 1305 burning aerosol measured from the C-130 aircraft during SAFARI 2000, *J. Geophys. Res.*,
 1306 108 (D13), 8473, doi:10.1029/2002JD002226, 2003.

1307 Hély, C., K. Caylor, S. Alleaume, R. J. Swap, and H. H. Shugart, Release of gaseous and
 1308 particulate carbonaceous compounds from biomass burning during the SAFARI 2000 dry
 1309 season field campaign, *J. Geophys. Res.*, 108 (D13), 8470, doi:10.1029/2002JD002482,
 1310 2003.

1311 Holben, B. N., T. F. Eck, I. Slutsker, D. Tanré, J. P. Buis, A. Setzer, E. Vermote, J. A. Reagan,
 1312 Y. J. Kaufman, T. Nakajima, F. Lavenu, I. Jankowiak and A. Smirnov, AERONET-A
 1313 federated instrument network and data archive for aerosol characterization, *Remote Sensing*
 1314 *of Environment*, 66(1), 1998.

1315 Hsu, N. C., J. R. Herman, O. Torres, B. N. Holben, D. Tanre, T. F. Eck, A. Smirnov, B.
 1316 Chatenet, and F. Lavenu, Comparisons of the TOMS aerosol index with Sun-photometer
 1317 aerosol optical thickness: Results and applications, *J. Geophys. Res.*, 104(D6), 6269-6279,
 1318 1999.

1319 Ichoku, C., L. A. Remer, Y. J. Kaufman, R. Levy, D. A. Chu, D. Tanré, and B. N. Holben,
 1320 MODIS observation of aerosols and estimation of aerosol radiative forcing over southern
 1321 Africa during SAFARI 2000, *J. Geophys. Res.*, 108 (D13), 8499,
 1322 doi:10.1029/2002JD002366, 2003.

1323 Intergovernmental Panel on Climate Change (IPCC), *Climate Change 2001: The Scientific Basis*,
 1324 Cambridge Univ. Press, New York, 2001.

1325 Jury, M., and T. Freiman, The climate of tropical southern Africa during the SAFARI 2000
 1326 campaign, *South African Journal of Science*, 98, 527, 2002.

1327 Kahn, R., P. Banerjee, D. McDonald, Sensitivity of multiangle imaging to natural mixtures of
 1328 aerosols over ocean, *J. Geophys. Res.*, 106(D16), 18219-18238, 10.1029/2000JD900497,
 1329 2001.

1330 Kalnay, E. et al., The NCEP/NCAR 40-year reanalysis project, *Bull. Am. Meteorol. Soc.*, 77,
 1331 437-471, 1996.

1332 Kaufman, Y. J., D. Tanré, L. A. Remer, E. F. Vermote, A. Chu, B. N. Holben, Operational

1333 remote sensing of tropospheric aerosol over land from EOS moderate resolution imaging
 1334 spectroradiometer, *J. Geophys. Res.*, 102(D14), 17051-17068, 10.1029/96JD03988, 1997.
 1335 Kaufman, Y., Ichoku, C., Giglio, L., Korontzi, S., Chu, D. A., Hao, W. M., Li, R.-R., and Justice,
 1336 C. O., Fires and smoke observed from the Earth Observing System MODIS instrument:
 1337 products, validation, and operational use. *International Journal of Remote Sensing*, 24:1765-
 1338 1781, 2003.
 1339 Kiehl, J., J. Hack, G. Bonan, B. Boville, B. Briegleb, D. Williamson, and P. Rasch, Description
 1340 of the NCAR Community Climate Model (CCM3), Tech. Rep. NCAR/TN-420+STR, Natl.
 1341 Center for Atmos. Res., Boulder, Colorado, 1996.
 1342 Korontzi, S., D.P. Roy, C.O. Justice and D.E. Ward, Modeling and sensitivity analysis of fire
 1343 emissions in southern Africa during SAFARI 2000, *Remote Sens. Environ.*, 92(3), 2004.
 1344 Lavoué, D., C. Liousse, H. Cachier, B. J. Stocks, J. G. Goldammer, Modeling of carbonaceous
 1345 particles emitted by boreal and temperate wildfires at northern latitudes, *J. Geophys. Res.*,
 1346 105(D22), 26871-26890, 10.1029/2000JD900180, 2000.
 1347 Lin, S.J., and R.B. Rood, Multidimensional flux-form semi-Lagrangian transport schemes, *Mon.*
 1348 *Wea. Rev.*, 124, 2046, 1996.
 1349 Liousse, C., J. E. Penner, C. Chuang, J. J. Walton, H. Eddleman, H. Cachier, A global three-
 1350 dimensional model study of carbonaceous aerosols, *J. Geophys. Res.*, 101(D14), 19411-
 1351 19432, 10.1029/95JD03426, 1996.
 1352 Magi, B. I., and P. V. Hobbs, Effects of humidity on aerosols in southern Africa during the
 1353 biomass burning season, *J. Geophys. Res.*, 108 (D13), 8495, doi:10.1029/2002JD002144,
 1354 2003.
 1355 Magi, B. I., P. V. Hobbs, B. Schmid, J. Redemann, Vertical profiles of light scattering, light

1356 absorption, and single scattering albedo during the dry, biomass burning season in southern
 1357 Africa and comparisons of in situ and remote sensing measurements of aerosol optical
 1358 depths, *J. Geophys. Res.*, 108 (D13), 8504, doi:10.1029/2002JD002361, 2003.

1359 Martonchik, J., D. Diner, R. Kahn, T. Ackerman, M. Verstraete, B. Pinty, and H. Gordon,
 1360 Techniques for the retrieval of aerosol properties over land and ocean using Multiangle
 1361 imaging, *IEEE Trans. Geosci. Remote Sens.*, 36, 1212-1227, 1998.

1362 Martonchik, J., D. Diner, K. Crean, and M. Bull, Regional aerosol retrieval results from MISR,
 1363 *IEEE Trans. Geosci. Remote Sens.*, 40, 1520-1531, 2002.

1364 McGill, M. J., D. L. Hlavka, W. D. Hart, E. J. Welton, and J. R. Campbell, Airborne lidar
 1365 measurements of aerosol optical properties during SAFARI-2000, *J. Geophys. Res.*, 108
 1366 (D13), 8493, doi:10.1029/2002JD002370, 2003.

1367 Myhre, G., T. K. Berntsen, J. M. Haywood, J. K. Sundet, B. N. Holben, M. Johnsrud, F. Stordal,
 1368 Modeling the solar radiative impact of aerosols from biomass burning during the Southern
 1369 African Regional Science Initiative (SAFARI-2000) experiment, *J. Geophys. Res.*, 108
 1370 (D13), 8501, doi:10.1029/2002JD002313, 2003.

1371 Pósfai M., R. Simonics, J. Li, P. V. Hobbs, and P. R. Buseck, Individual aerosol particles from
 1372 biomass burning in southern Africa: 1. Compositions and size distributions of carbonaceous
 1373 particles, *J. Geophys. Res.*, 108 (D13), 8483, doi:10.1029/2002JD002291, 2003.

1374 Prupacher, H.R., and J.D. Klett, Microphysics of Clouds and Precipitation, Kluwer Academic
 1375 Publishers, 1997.

1376 Rasch, P. J., N. M. Mahowald, B. E. Eaton, Representations of transport, convection, and the
 1377 hydrologic cycle in chemical transport models: Implications for the modeling of short-lived
 1378 and soluble species, *J. Geophys. Res.*, 102(D23), 28127-28138, 10.1029/97JD02087, 1997.

1379 Reid, J. S., P. V. Hobbs, C. Lioussé, J. V. Martins, R. E. Weiss, T. F. Eck, Comparisons of
 1380 techniques for measuring shortwave absorption and black carbon content of aerosols from
 1381 biomass burning in Brazil, *J. Geophys. Res.*, 103(D24), 32031-32040, 10.1029/98JD00773,
 1382 1998.

1383 Reid, J. S., P. V. Hobbs, R. J. Ferek, D. R. Blake, J. V. Martins, M. R. Dunlap, C. Lioussé,
 1384 Physical, chemical, and optical properties of regional hazes dominated by smoke in Brazil, *J.*
 1385 *Geophys. Res.*, 103(D24), 32059-32080, 10.1029/98JD00458, 1998.

1386 Reid, J., R. Koppmann, T. Eck, and D. Eleuterio, A review of biomass burning emissions, part II:
 1387 Intensive physical properties of biomass burning particles, *Atmospheric Chemistry and*
 1388 *Physics Discussions*, 4, 2004.

1389 Schmid B., et al., Coordinated airborne, spaceborne, and ground-based measurements of massive
 1390 thick aerosol layers during the dry season in southern Africa, *J. Geophys. Res.*, 108 (D13),
 1391 8496, doi:10.1029/2002JD002297, 2003.

1392 Scholes, R. J., J. Kendall, C. O. Justice, The quantity of biomass burned in southern Africa, *J.*
 1393 *Geophys. Res.*, 101(D19), 23667-23676, 10.1029/96JD01623, 1996.

1394 Scholes, M and M. O. Andreae, Biogenic and pyrogenic emissions from Africa and their impact
 1395 on the global atmosphere, *Ambio*, 29, 23-29, 2000.

1396 Seinfeld, J.H., and S.N. Pandis, Atmospheric Chemistry and Physics: From Air Pollution to
 1397 Climate Change, John Wiley & Sons, 1998.

1398 Shao, Y., Physics and Modeling of Wind Erosion, Kluwer Acad., Norwell, Mass., 2000.

1399 Sinha P., P. V. Hobbs, R. J. Yokelson, I. T. Bertschi, D. R. Blake, I. J. Simpson, S. Gao, T. W.
 1400 Kirchstetter, and T. Novakov, Emissions of trace gases and particles from savanna fires in
 1401 southern Africa, *J. Geophys. Res.*, 108 (D13), 8487, doi:10.1029/2002JD002325, 2003.

1402 Smirnov A., B.N.Holben, T.F.Eck, O.Dubovik, and I.Slutsker, Cloud screening and quality
 1403 control algorithms for the AERONET database, *Rem. Sens. Env.*, 73, 337-349, 2000.
 1404 Spinhirne, J. D., J. Rall and V.S. Scott, Compact eye safe lidar systems, *Rev. Laser, Eng.*, 23,
 1405 112-118, 1995.
 1406 Stein D. C., R. J. Swap, S. Greco, S. J. Piketh, S. A. Macko, B. G. Doddridge, T. Elias, R. T.
 1407 Bruintjes, Haze layer characterization and associated meteorological controls along the
 1408 eastern coastal region of southern Africa, *J. Geophys. Res.*, 108 (D13), 8506,
 1409 doi:10.1029/2002JD003237, 2003.
 1410 Swap R. J., H. J. Annegarn, J. T. Suttles, M. D. King, S. Platnick, J. L. Privette, R. J. Scholes,
 1411 Africa burning: A thematic analysis of the Southern African Regional Science Initiative
 1412 (SAFARI 2000), *J. Geophys. Res.*, 108 (D13), 8465, doi:10.1029/2003JD003747, 2003.
 1413 Tanré, D., Y. J. Kaufman, M. Herman, S. Mattoo, Remote sensing of aerosol properties over
 1414 oceans using the MODIS/EOS spectral radiances, *J. Geophys. Res.*, 102(D14), 16971-16988,
 1415 10.1029/96JD03437, 1997.
 1416 Toon, O. B., R. Turco, D. Westphal, R. Malone, and M. Liu, A multidimensional model for
 1417 aerosols: Description of computational analogs, *J. Atmospheric Science*, 45, 2123, 1988.
 1418 Torres, O., P. K. Bhartia, J. R. Herman, Z. Ahmad, J. Gleason, Derivation of aerosol properties
 1419 from satellite measurements of backscattered ultraviolet radiation: Theoretical basis, *J.*
 1420 *Geophys. Res.*, 103(D14), 17099-17110, 10.1029/98JD00900, 1998.
 1421 Torres, O, P. Bhartia, A. Sinyuk, E. Welton, and B. Holben, Total Ozone Mapping Spectrometer
 1422 measurements of aerosol absorption from space: Comparison to SAFARI 2000 ground-based
 1423 observations, *J. Geophys. Res.*, 110(D10S18), doi:10.1029/2004JD004611, 2005.

1424 Twitty, J. and J. Weinman, Radiative properties of carbonaceous aerosols, *J. Applied*
 1425 *Meteorology*, 10, 1971.
 1426 van der Werf, G. R., J. T. Randerson, J. Collatz, and L. Giglios, Carbon emissions from fires in
 1427 tropical and subtropical ecosystems, *Global Change Biology*, 9(4), 547,
 1428 doi:10.1046/j.1365-2486.2003.00604, 2003.
 1429 Warner, J. and S. Twomey, The production of cloud nuclei by cane fires and the effect on cloud
 1430 drop concentrations, *J. Atmos. Sci.*, 24, 704-706, 1967.
 1431 Welton, E. T., J. R. Campbell, J. D. Spinhirne, and V. S. Scott, Global monitoring of clouds and
 1432 aerosols using a network of micro-pulse lidar systems, *Proc. SPIE Int. Soc. Opt. Eng.*, 4153,
 1433 151-158, 2001.
 1434 Westphal, D. L., O. B. Toon, Simulations of microphysical, radiative, and dynamical processes
 1435 in a continental-scale forest fire smoke plume, *J. Geophys. Res.*, 96(D12), 22379-22400,
 1436 10.1029/91JD01956, 1991a.
 1437 Westphal, D. L., O. B. Toon, The short-term temperature response to smoke from oil fires,
 1438 *Geophys. Res. Lett.*, 18(10), 1873-1876, 10.1029/91GL02239, 1991b.
 1439 Wiscombe, W., "Mie scattering calculations: Advances in technique and fast, vector-speed
 1440 computer codes," NCAR Technical Note, TN-140+STR, 1979.
 1441 Wong, J. and Z. Li, Retrieval of Optical Depth for Heavy Smoke Aerosol Plumes: Uncertainties
 1442 and Sensitivities to the Optical Properties, *J. Atmospheric Sciences*, 59(3), 250-261, 2002.
 1443 Yokelson, R., D. Griffith, D. Ward, Open-path Fourier transform infrared studies of large-scale
 1444 laboratory biomass fires, *J. Geophys. Res.*, 101(D15), 21067-21080, 1996.
 1445 Zhang, L., S. Gong, J. Padro, L. Barrie, A size-segregated particle dry deposition scheme for an
 1446 atmospheric aerosol module, *Atmospheric Environment*, 35(3), 549-560, 2001.

1447 Table Captions

1448 Table 1. Input Parameters used in Base Model

1449 Table 2. Monthly mean AOT_{500} , $\alpha_{[380/440]}$, $\alpha'_{[380/500/870]}$, SSA_{440} , SSA_{670} , SSA_{870} , SSA_{1020} of
1450 smoke dominated days from various simulations and AERONET at Inhaca and Ndola for
1451 September 2000.

1452 Table 3. Presents the number of days included in the mean AOT and the mean AOT observed by
1453 AERONET, MISR, MODIS, and simulated by the base model at the six study sites for
1454 September 2000.

1455 Table 4. Presents the number of days included in the mean AOT and the mean AOT observed by
1456 AERONET, EP-TOMS, and simulated by the base model at the six study sites for September
1457 2000.

1458 Table 5. Sensitivity test names and modifications made relative to Base Model.

1459 Figure Captions

1460 Figure 1a. Satellite image of the “River of Smoke” on 4 September 2000. This image shows an
1461 example of biomass burning aerosols being transported across southern Africa and over the
1462 Indian Ocean [Swap *et al.* [2003], SeaWiFS Project, NASA/Goddard Space Flight Center, and
1463 ORBIMAGE].

1464 Figure 1b. Simulated daily mean AOT at 550 nm on 4 September 2000.

1465 Figure 2. Vertically column-integrated volume size distributions used in the simulations
1466 conducted in this study. The solid black line represents the base model particle size distribution
1467 fitted to parameters from an AERONET almucantar scan at Ndola, Zambia on 16 September
1468 2000. The gray dashed line represents the PCASP model size distribution fitted to parameters
1469 from mean PCASP measurements at Otavi, Namibia on 13 September 2000. The gray solid line
1470 represents the AERONET-Mean model size distribution fitted to parameters from the mean
1471 AERONET almucantar scans at Ndola, Zambia on smoke dominated days in September 2000.
1472 The gray dashed line represents the 22-Bins model size distribution. The parameters for each of
1473 the models are listed in Tables 1 and 4.

1474 Figure 3. Mean interpolated aerosol emissions using GFED dataset for September 2000 and
1475 locations where the data used in our paper was collected.

1476 Figure 4. Daily mean AOT₅₀₀ simulated by the base model (solid line) and Daily Emissions
1477 model (dashed line), and all AOT₅₀₀ retrievals from AERONET (+) at each study site for
1478 September 2000.

1479 Figure 5. Scatterplot of daily mean AOT₅₀₀ retrieved by AERONET versus simulated daily
1480 mean AOT₅₀₀ for smoke dominated days at the six study sites for September 2000. The dashed
1481 line represents the 1-to-1 line and the solid line represents the line of best fit through all points.

1482 The equation of the line of best fit and correlation coefficient (R) is reported in the figure. Each
 1483 study site is represented by a different symbol: Etosha Pan (square), Inhaca (triangle), Mongu
 1484 (diamond), Ndola (plus sign), Senanga (asterisk), and Skukuza (cross).

1485 Figure 6. Scatterplot of daily mean SSA_{440} retrieved by AERONET versus simulated daily mean
 1486 SSA_{440} for smoke dominated days at the six study sites for September 2000. The dashed line
 1487 represents the 1-to-1 line and the solid line represents the line of best fit through all points. The
 1488 equation of the line of best fit and correlation coefficient (R) is reported in the figure. Each study
 1489 site is represented by a different symbol: Etosha Pan (square), Inhaca (triangle), Mongu
 1490 (diamond), Ndola (plus sign), Senanga (asterisk), and Skukuza (cross). The single bar at the top-
 1491 left represents the error in the AERONET retrievals of ± 0.03 .

1492 Figure 7. Scatterplot of daily mean Ångström exponent [440/870 nm] retrieved by AERONET
 1493 versus simulated daily mean Ångström exponent [440/870 nm] for smoke dominated days at the
 1494 six study sites for September 2000. The dashed line represents the 1-to-1 line and the solid line
 1495 represents the line of best fit through all points. The equation of the line of best fit and
 1496 correlation coefficient (R) is reported in the figure. Each study site is represented by a different
 1497 symbol: Etosha Pan (square), Inhaca (triangle), Mongu (diamond), Ndola (plus sign), Senanga
 1498 (asterisk), and Skukuza (cross).

1499 Figure 8. Monthly mean spectral dependence of AOT of smoke dominated days for September
 1500 2000 at Inhaca and Ndola. The solid lines represent the results from the base model and the
 1501 asterisks connected with a dashed line represent the AERONET retrievals.

1502 Figure 9. Monthly mean spectral dependence of SSA of smoke dominated days for September
 1503 2000 at Inhaca and Ndola. The solid lines represent the results from the base model and the
 1504 asterisks connected with a dashed line represent the AERONET retrievals.

1505 Figure 10. Mean extinction profiles at Mongu and Senanga on 6 September 2000. The simulated
1506 profiles represent the average of the results at 0600 and 1200 timesteps, the CPL profiles
1507 represents the average of four samples between 0800 and 1100 UTC (black line), and the AATS
1508 profiles represent one sample around 0900 UTC (red line). The blue line represents the
1509 simulated results from the base model, and the green line represents the simulated results from
1510 the 3-Layers model.

1511 Figure 11. Mean extinction profiles at Skukuza for September 2000. Mean includes: 1-3, 6, 7, 9,
1512 10, 13, 14, 17 September 2000. Base model is represented by the solid black line, 3-Layers
1513 model is represented by the solid red line, 2 km-Layer model is represented by the solid blue
1514 line, and MPL retrievals are represented by the dashed line.

1515 Figure 12. Comparisons of monthly mean AOT_{550} observed by MODIS (left) and simulated by
1516 our base model (right) for September 2000 over southern Africa. The hatch marks represent
1517 locations with no data (N.D.).

1518 Figure 13. Comparisons of monthly mean AOT_{550} observed by MISR (left) and simulated by our
1519 base model (right) for September 2000 over southern Africa. The hatch marks represent locations
1520 with no data (N.D.).

1521 Figure 14. Comparisons of monthly mean AOT_{380} observed by EP-TOMS (left) and simulated by
1522 our base model (right) for September 2000 over southern Africa. The hatch marks represent
1523 locations with no data (N.D.).

1524 Figure 15. Scatterplots of monthly mean AOT_{550} observed by MODIS versus model. The domain
1525 is divided into to two regions: land (left) and ocean (right). The dashed line represents the 1-to-1
1526 line and the solid line represents the line of best fit.

1527 Figure 16. Scatterplots of monthly mean AOT_{550} observed by MISR versus model. The domain
 1528 is divided into to two regions: land (left) and ocean (right). The dashed line represents the 1-to-1
 1529 line and the solid line represents the line of best fit.

1530 Figure 17. Scatterplots of monthly mean AOT_{380} observed by EP-TOMS versus model. The
 1531 domain is divided into to two regions: land (left) and ocean (right). The dashed line represents
 1532 the 1-to-1 line and the solid line represents the line of best fit.

1533 Figure 18. Scatterplots of monthly mean AOT_{550} observed by MODIS versus MISR at points
 1534 over land (left) and ocean (right) for September 2000. The dashed line represents the 1-to-1 line
 1535 and the solid line represents the line of best fit.

1536 Figure 19. Scatterplots of monthly mean EP-TOMS AI versus simulated monthly mean AOT_{380}
 1537 for September 2000. The geographic domain is restricted to a region dominated by biomass
 1538 burning aerosols (5°S to 20°S and 10°W to 35°E) and then separated into land (left) and ocean
 1539 (right) points. The solid lines in both figures represent the line of best fit. The dashed line in land
 1540 plot represents the regression line from the comparison of AERONET AOT_{380} and EP-TOMS AI
 1541 over smoke dominated locations in September 2000.

1542 Figure 20. Daily mean column-integrated volume size distribution simulated by the base model
 1543 (solid line) and the daily mean column-integrated volume size distribution fitted to parameters
 1544 from AERONET almucantar scans (dashed line) at Etosha Pan on 13 September 2000. The
 1545 model size distribution is normalized to the fine volume concentration of the AERONET
 1546 retrieval.

1547 Figure 21. Daily mean volume size distribution simulated by the base model (solid line) and the
 1548 volume size distribution fitted to parameters reported by *Haywood et al.* [2003] which are
 1549 representative of average PCASP measurements within an aged smoke (dashed line) at Etosha

1550 Pan on 13 September 2000. The model size distribution is normalized to the fine volume
1551 concentration of the PCASP measurement.

1552 Figure 22. Normalized column-integrated daily mean volume size distributions at Ndola, Zambia
1553 on 16 September 2000. The model size distributions are normalized to the fine volume
1554 concentration of the AERONET retrieval. The black solid line represents the base model, gray
1555 solid line represents the PCASP model, and the dashed black line represents the AERONET
1556 retrieval.

1557 Figure 23. Normalized daily mean column-integrated AERONET and simulated volume size
1558 distributions at Ndola, Zambia on 16 September 2000. The model size distributions are
1559 normalized to the fine volume concentration of the AERONET retrieval. The solid black line
1560 represents the base model, gray line represents Density model, the gray dashed line represents
1561 the No Dry Dep. model, and the dashed black line represents the AERONET retrieval.

1562 Figure 24. AERONET and simulated mean spectral dependence of SSA of smoke dominated
1563 days for September 2000 at Inhaca and Ndola. The solid line represents the results from the Base
1564 model, the dotted line represents the WD-AERONET model, the dashed-dotted line represents
1565 the WI-AERONET model, the dashed line represents the WD-AERONET-Mean model, and the
1566 asterisks connected with dashed line represent the AERONET retrievals.

Table 1. Input Parameters used in Base Model.

Microphysical Processes	Advection Coagulation Dry Deposition Wet Removal Sedimentation					
Emission Dataset	GFED [van der Werf et al., 2003]		Emission Factor: 10 g TPM/kg of DM			
Emission Rate over Entire Model Domain	Constant throughout month		August: 2.05e-7 g cm ⁻² s ⁻¹ September: 3.64e-7 g cm ⁻² s ⁻¹			
Injection Height	Mixed between Surface & PBLH		Peak height of the MATCH PBL ranged between 1 km and 3.7 km at the study six sites			
Diurnal Cycle	Aerosol emitted for 12-hour period during daylight hours					
Particle Density	1.35 g cm ⁻³					
Initial Size Distribution	Radius Range [μm]	# Bins	Mode	N _f	r _N [μm]	c
	0.01 to 10	16	1	0.99986	0.079	1.5
			2	0.00014	0.695	2.1
Dependence of Size on Relative Humidity	Follows parameterization described by Magi & Hobbs [2003]					
Refractive Index	Wavelength independent		N _{ref} = 1.51-0.024i			

Table 2. Monthly mean AOT_{500} , $\alpha_{[380/440]}$, $\alpha'_{[380/500/870]}$, SSA_{440} , SSA_{670} , SSA_{870} , and SSA_{1020} of smoke dominated days from various simulations and AERONET at Inhaca and Ndola for September 2000.

Site	Case	AOT [500]	α [380/440]	α' [380/500/870]	SSA [440]	SSA [670]	SSA [870]	SSA [1020]
Inhaca	AERONET	0.49	1.30	0.41	0.89	0.87	0.85	0.8
	Base	0.54	1.28	1.31	0.89	0.86	0.83	0.8
	Mass	0.78	1.27	1.11	0.82	0.78	0.73	0.7
Ndola	AERONET	0.78	1.43	1.23	0.87	0.85	0.82	0.8
	Base	0.59	1.38	1.24	0.89	0.86	0.82	0.7
	Mass	0.89	1.27	1.11	0.83	0.79	0.73	0.7
	22 - Bins	0.61	1.32	1.38	0.89	0.86	0.83	0.8
	AERONET - Mean	0.58	1.46	1.23	0.89	0.85	0.81	0.7
	PCASP	0.43	1.66	0.64	0.87	0.82	0.78	0.7
	No Coagulation	0.55	1.52	1.11	0.88	0.85	0.81	0.7
	WI - Haywood et al. [2003]	0.64	1.29	1.36	0.89	0.86	0.83	0.8
	WI - AERONET	0.60	1.38	1.31	0.91	0.88	0.86	0.8
	WD - AERONET	0.60	1.38	1.21	0.91	0.90	0.87	0.8
	WD - AERONET - Mean	0.59	1.38	1.15	0.89	0.88	0.85	0.8
	No RH	0.54	1.36	1.22	0.88	0.84	0.80	0.7
	Density	1.23	1.25	1.27	0.89	0.86	0.83	0.8
	Shape	0.58	1.38	1.20	0.89	0.86	0.82	0.7
	No Dry Dep.	0.62	1.35	1.19	0.89	0.85	0.82	0.7
	Zhang et al. [2001]	0.56	1.36	1.20	0.89	0.86	0.82	0.7

1571 Table 3. Presents the number of days included in the mean AOT and the mean AOT observed by
 1572 AERONET, MISR, MODIS, and simulated by the base model at the six study sites for September 2000.

Site	# of Days	Model [550]	MISR [550]	MODIS [550]	AERONET [500]
Etosha Pan	7	0.38	0.37	0.68	0.51
Inhaca	6	0.36	0.28	0.37	0.38
Mongu	7	0.59	0.54	0.65	0.79
Ndola	6	0.49	0.47	0.62	0.80
Senanga	7	0.60	0.54	0.73	0.75
Skukuza	5	0.46	0.37	0.47	0.30

1573 Table 4. Presents the number of days included in the mean AOT and the mean AOT observed by
 1574 AERONET, EP-TOMS, and simulated by the base model at the six study sites for September 2000.
 1575

Site	# of Days	Model [380]	EP-TOMS [380]	AERONET [380]
Etosha Pan	23	0.50	0.71	0.54
Inhaca	11	0.61	0.51	0.58
Mongu	20	1.05	1.18	1.35
Ndola	18	1.02	1.11	1.15
Senanga	18	1.07	0.83	1.16
Skukuza	11	0.67	0.53	0.69

1576

Table 5. Sensitivity test names and modifications made relative to Base Model.

Model Name	Parameter Changed in Base Model	New Parameter			
PCASP	Size Distribution (Mode/Number Fraction/Radius[N]/Std. Dev.)	1	0.9957	0.10 μm	1.3
		2	0.0041	0.22 μm	1.5
		3	0.0002	1.00 μm	1.9
AERONET - Mean	Size Distribution (Mode/Number Fraction/Radius[N]/Std. Dev.)	1	0.9999	0.08 μm	1.5
		2	0.0001	0.73 μm	2.1
Mass	Size Distribution	Transport mass following <i>Chin et al.</i> [2001]			
22 - Bins	Radius Range	0.05 to 15 μm			
	Number of Size Bins	22 Size Bins			
3 Layers	Injection Height	Aerosols emitted in three model layers (1.5/3/5 km)			
2 km-Layer	Injection Height	Aerosols emitted in one model layer (2 km)			
No DC	Diurnal Cycle	Aerosols emitted evenly throughout the day			
1500 UTC	Diurnal Cycle	Aerosols emitted at 1500 UTC time step each day			
Daily Emissions	Emission Rate	GFED emissions linked to ATSR Fire Count Data			
No Coagulation	Microphysical Process	No Coagulation			
No RH	Relative Humidity	Relative Humidity assumed to be zero			
WI – Haywood et al. [2003]	Refractive Index (λ/N_{ref})	Wavelength Independent		1.54-0.025 <i>i</i>	
WI – AERONET	Refractive Index (λ/N_{ref})	Wavelength Independent		1.52-0.019 <i>i</i>	
WD – AERONET– Mean	Refractive Index (λ/N_{ref})	380 nm		1.51-0.024 <i>i</i>	
		440 nm		1.51-0.024 <i>i</i>	
		670 nm		1.52-0.020 <i>i</i>	
		870 nm		1.53-0.020 <i>i</i>	
		1020 nm		1.54-0.016 <i>i</i>	
WD – AERONET	Refractive Index (λ/N_{ref})	380 nm		1.52-0.019 <i>i</i>	
		440 nm		1.52-0.019 <i>i</i>	
		670 nm		1.52-0.016 <i>i</i>	
		870 nm		1.53-0.017 <i>i</i>	
		1020 nm		1.53-0.016 <i>i</i>	
Density	Density of Particle	Density: 0.675 g/cm ³			
Shape	Shape of Particle	Particle Shape: Flat Plates			
No Dry Dep.	Microphysical Process	No dry deposition in model			
Zhang et al. [2001]	Microphysical Process	Dry deposition routine from <i>Zhang et al.</i> [2001]			

Figure 1a. Satellite image of the “River of Smoke” on 4 September 2000. This image shows an example of biomass burning aerosols being transported across southern Africa and over the Indian Ocean [Swap *et al.* [2003], SeaWiFS Project, NASA/Goddard Space Flight Center, and ORBIMAGE].

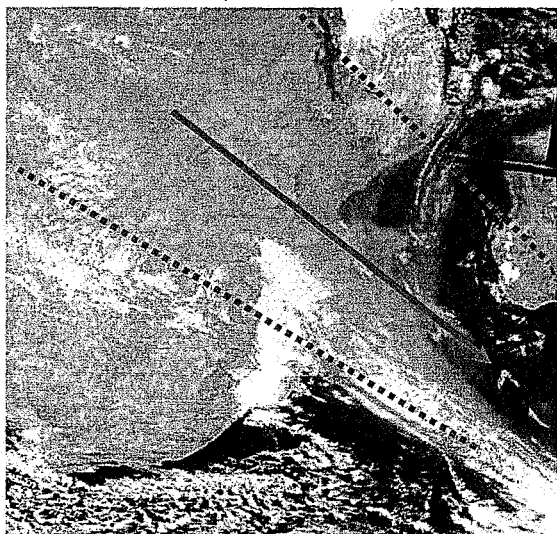


Figure 1b. Simulated daily mean AOT at 550 nm on 4 September 2000.

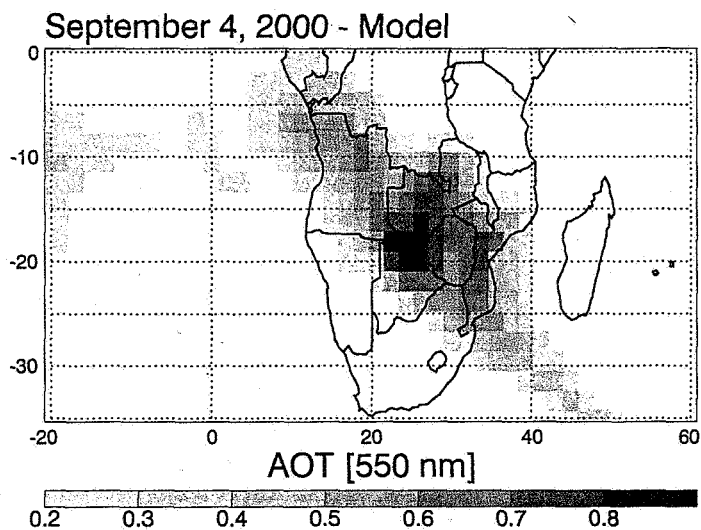


Figure 2. Vertically column-integrated volume size distributions used in the simulations conducted in this study. The solid black line represents the base model particle size distribution fitted to parameters from an AERONET almucantar scan at Ndola, Zambia on 16 September 2000. The gray dashed line represents the PCASP model size distribution fitted to parameters from mean PCASP measurements at Otavi, Namibia on 13 September 2000. The gray solid line represents the AERONET-Mean model size distribution fitted to parameters from the mean AERONET almucantar scans at Ndola, Zambia on smoke dominated days in September 2000. The gray dashed line represents the 22-Bins model size distribution. The parameters for each of the models are listed in Tables 1 and 4.

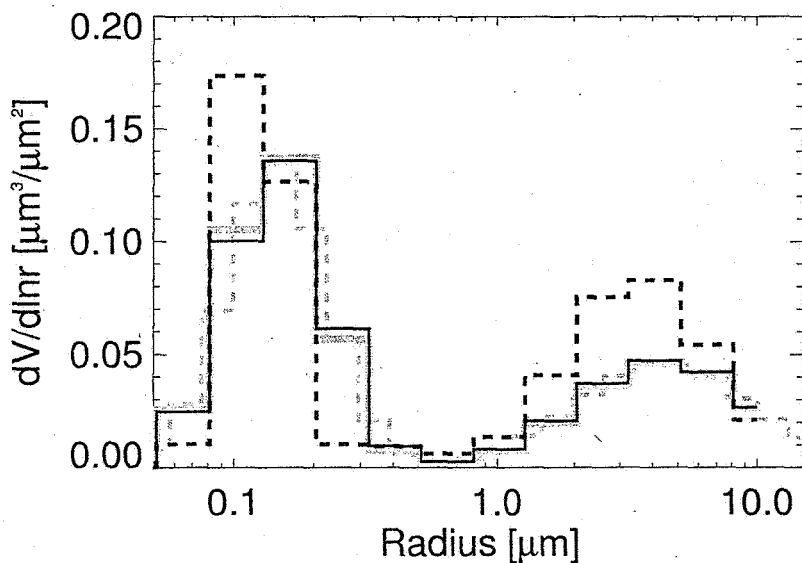


Figure 3. Mean interpolated aerosol emissions using GFED dataset for September 2000 and locations where the data used in our paper was collected.

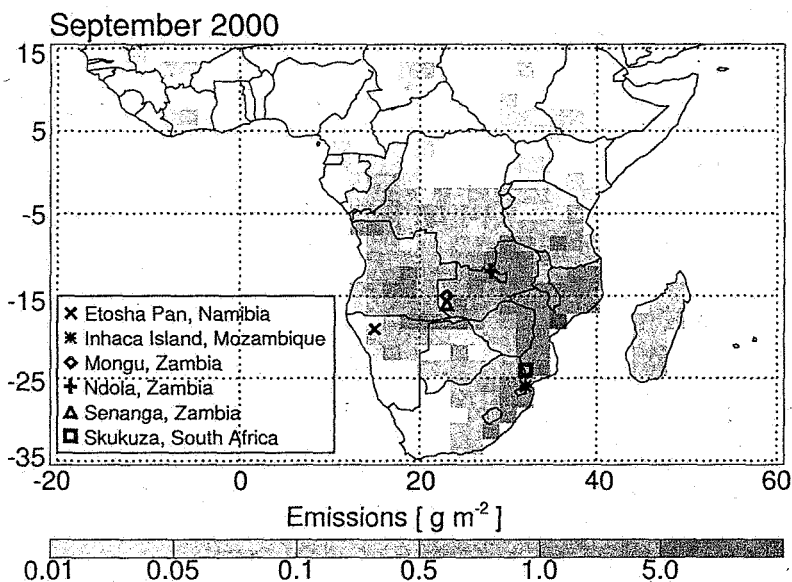


Figure 4. Daily mean AOT₅₀₀ simulated by the base model (solid line) and Daily Emissions model (dashed line), and all AOT₅₀₀ retrievals from AERONET (+) at each study site for September 2000.

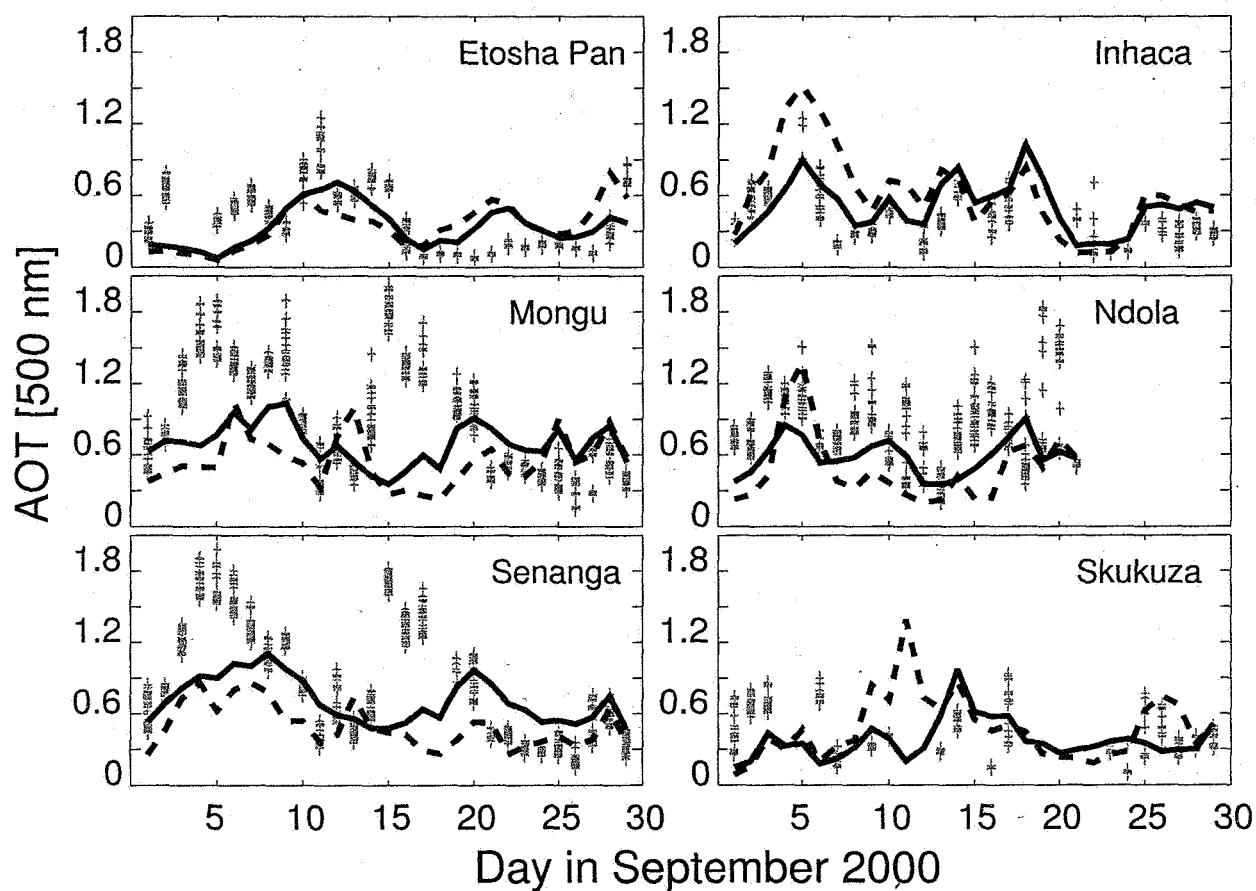


Figure 5. Scatterplot of daily mean AOT₅₀₀ retrieved by AERONET versus simulated daily mean AOT₅₀₀ for smoke dominated days at the six study sites for September 2000. The dashed line represents the 1-to-1 line and the solid line represents the line of best fit through all points. The equation of the line of best fit and correlation coefficient (R) is reported in the figure. Each study site is represented by a different symbol: Etosha Pan (square), Inhaca (triangle), Mongu (diamond), Ndola (plus sign), Senanga (asterisk), and Skukuza (cross).

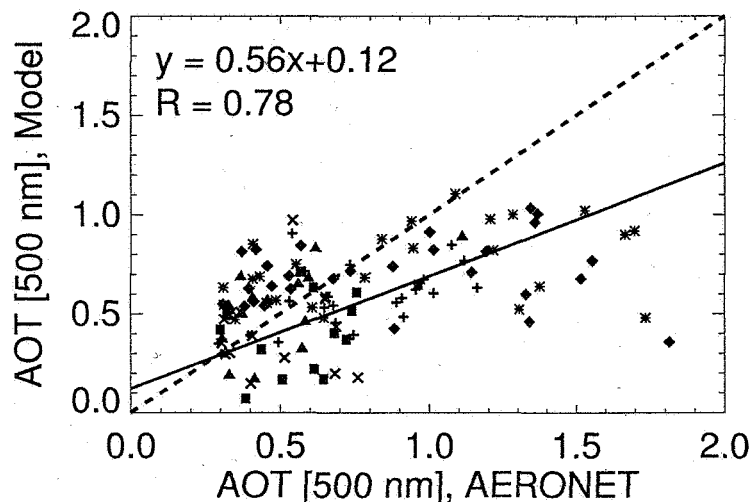


Figure 6. Scatterplot of daily mean SSA₄₄₀ retrieved by AERONET versus simulated daily mean SSA₄₄₀ for smoke dominated days at the six study sites for September 2000. The dashed line represents the 1-to-1 line and the solid line represents the line of best fit through all points. The equation of the line of best fit and correlation coefficient (R) is reported in the figure. Each study site is represented by a different symbol: Etosha Pan (square), Inhaca (triangle), Mongu (diamond), Ndola (plus sign), Senanga (asterisk), and Skukuza (cross). The single bar at the top-left represents the error in the AERONET retrievals of ± 0.03 .

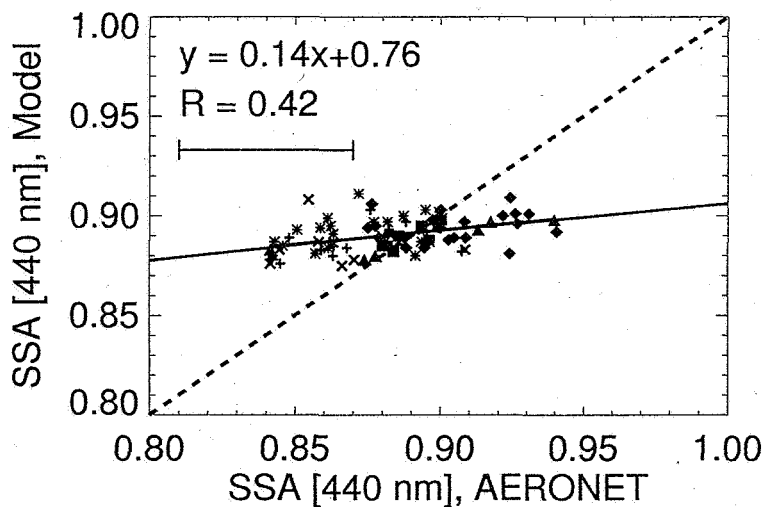


Figure 7. Scatterplot of daily mean Ångström exponent [440/870 nm] retrieved by AERONET versus simulated daily mean Ångström exponent [440/870 nm] for smoke dominated days at the six study sites for September 2000. The dashed line represents the 1-to-1 line and the solid line represents the line of best fit through all points. The equation of the line of best fit and correlation coefficient (R) is reported in the figure. Each study site is represented by a different symbol: Etosha Pan (square), Inhaca (triangle), Mongu (diamond), Ndola (plus sign), Senanga (asterisk), and Skukuza (cross).

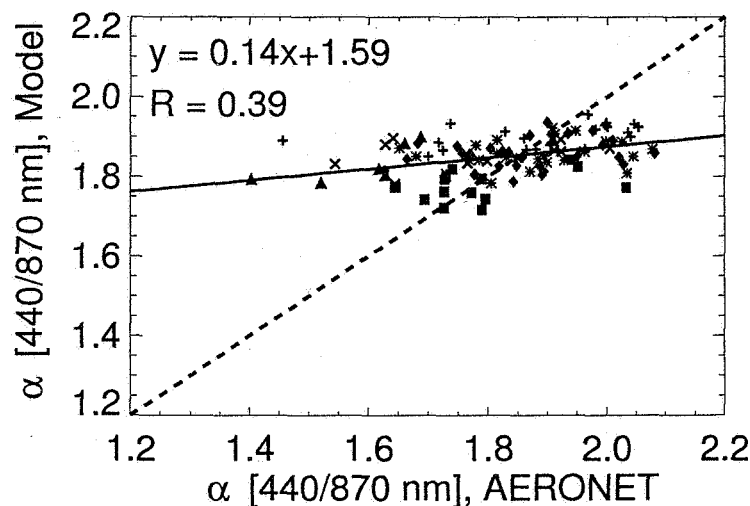


Figure 8. Monthly mean spectral dependence of AOT of smoke dominated days for September 2000 at Inhaca and Ndola. The solid lines represent the results from the base model and the asterisks connected with a dashed line represent the AERONET retrievals.

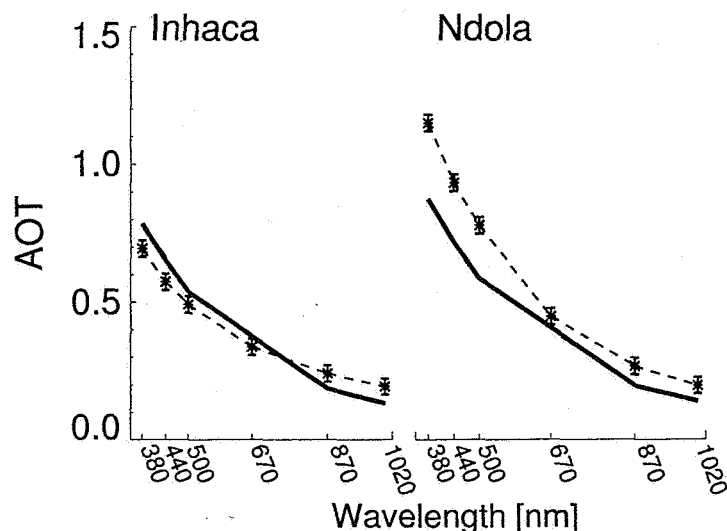


Figure 9. Monthly mean spectral dependence of SSA of smoke dominated days for September, 2000 at Inhaca and Ndola. The solid lines represent the results from the base model and the asterisks connected with a dashed line represent the AERONET retrievals.

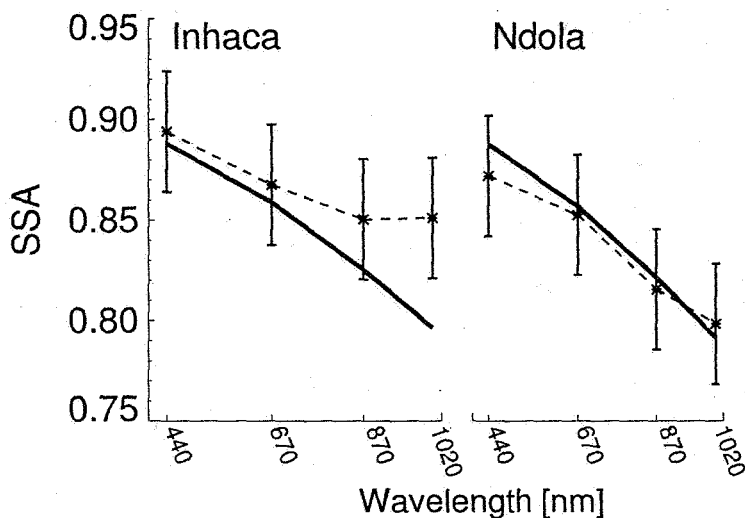
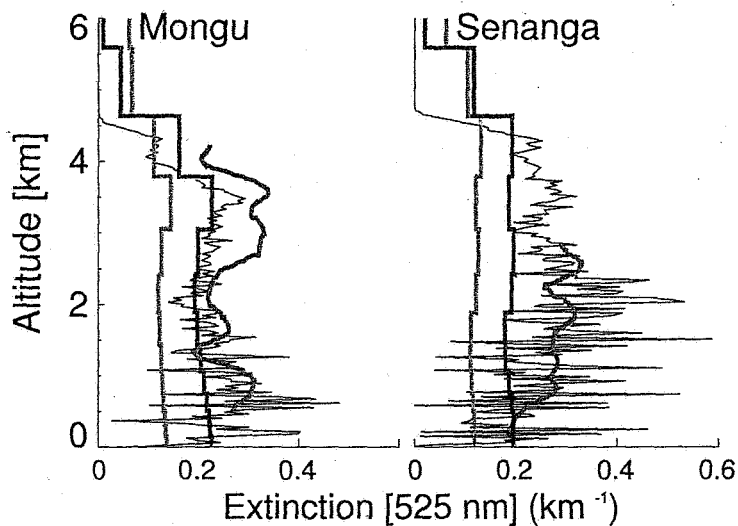
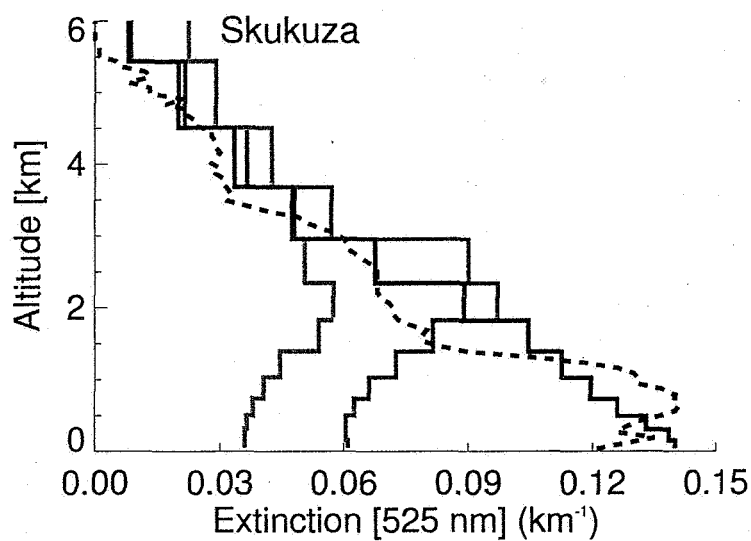


Figure 10. Mean extinction profiles at Mongu and Senanga on 6 September 2000. The simulated profiles represent the average of the results at 0600 and 1200 timesteps, the CPL profiles represents the average of four samples between 0800 and 1100 UTC (black line), and the AATS profiles represent one sample around 0900 UTC (red line). The blue line represents the simulated results from the base model, and the green line represents the simulated results from the 3-Layers model.



1669 Figure 11. Mean extinction profiles at Skukuza for September 2000. Mean includes: 1-3, 6, 7, 9,
 1670 10, 13, 14, 17 September 2000. Base model is represented by the solid black line, 3-Layers
 1671 model is represented by the solid red line, 2 km-Layer model is represented by the solid blue
 1672 line, and MPL retrievals are represented by the dashed line.



1673
 1674

Figure 12. Comparisons of monthly mean AOT_{550} observed by MODIS (left) and simulated by our base model (right) for September 2000 over southern Africa. The hatch marks represent locations with no data (N.D.).

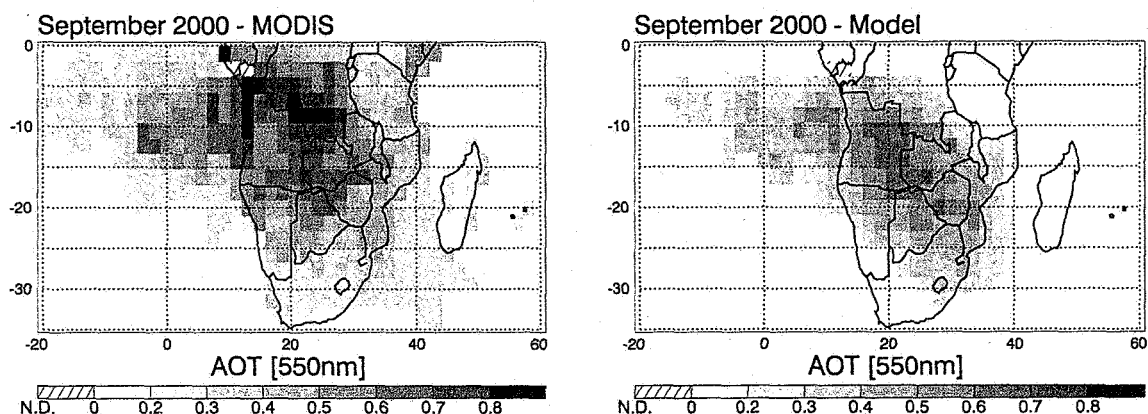


Figure 13. Comparisons of monthly mean AOT_{550} observed by MISR (left) and simulated by our base model (right) for September 2000 over southern Africa. The hatch marks represent locations with no data (N.D.).

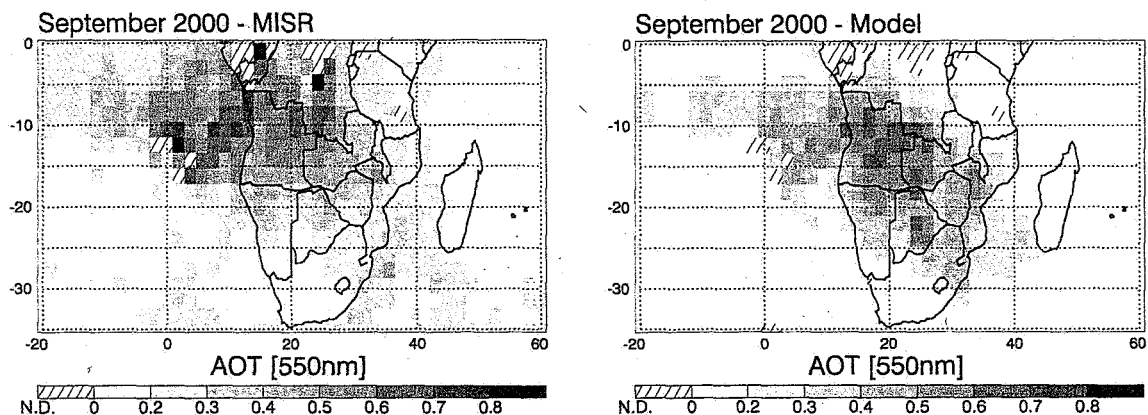


Figure 14. Comparisons of monthly mean AOT_{380} observed by EP-TOMS (left) and simulated by our base model (right) for September 2000 over southern Africa. The hatch marks represent locations with no data (N.D.).

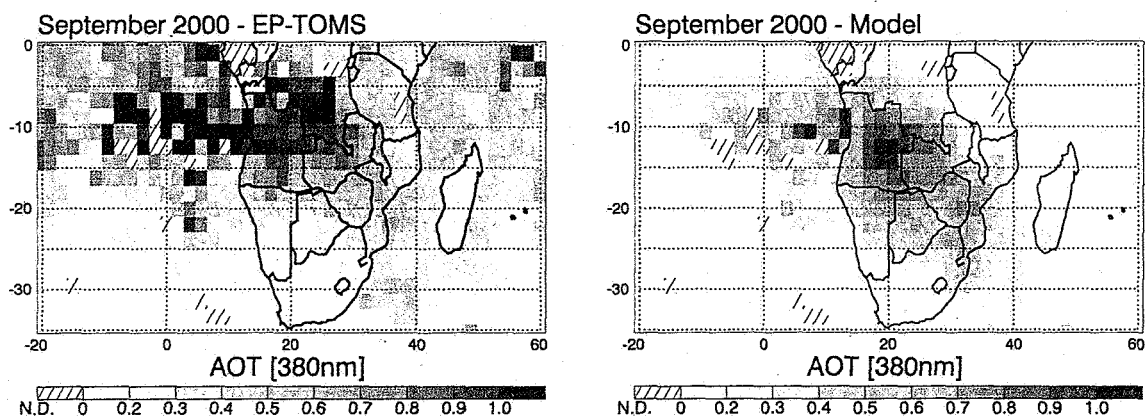


Figure 15. Scatterplots of monthly mean AOT₅₅₀ observed by MODIS versus model. The domain is divided into two regions: land (left) and ocean (right). The dashed line represents the 1-to-1 line and the solid line represents the line of best fit.

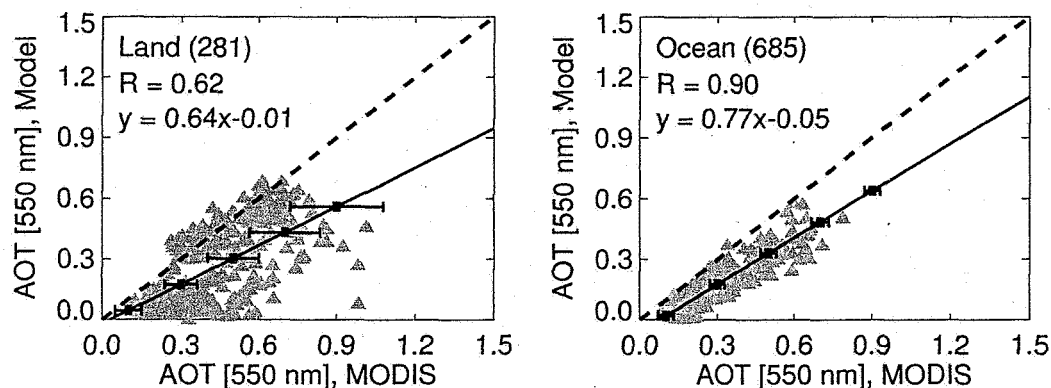


Figure 16. Scatterplots of monthly mean AOT₅₅₀ observed by MISR versus model. The domain is divided into two regions: land (left) and ocean (right). The dashed line represents the 1-to-1 line and the solid line represents the line of best fit.

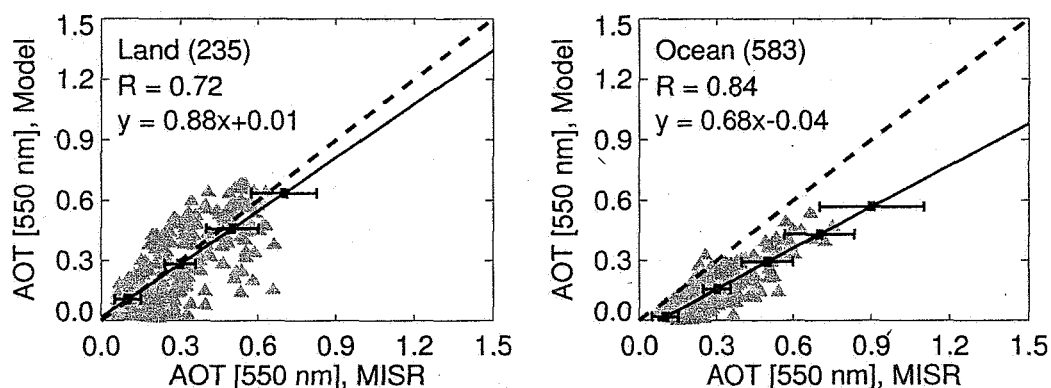
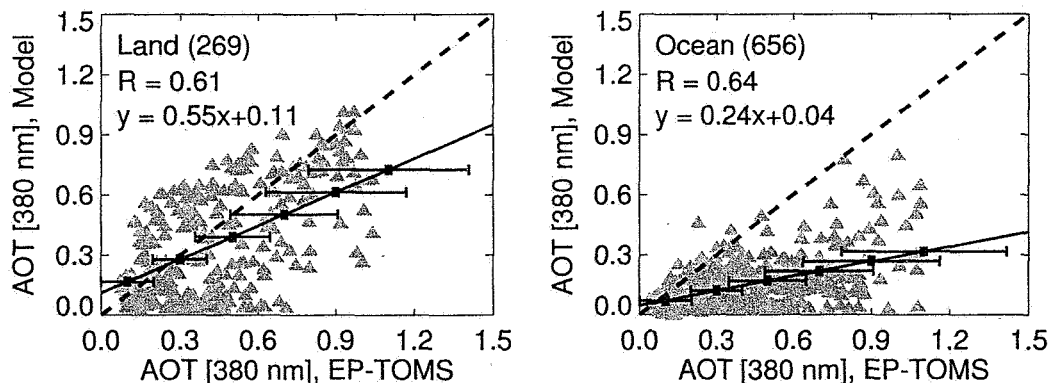
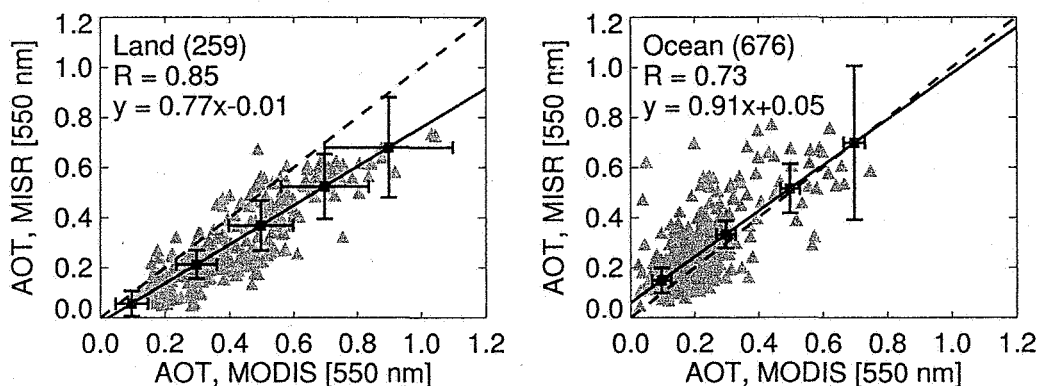


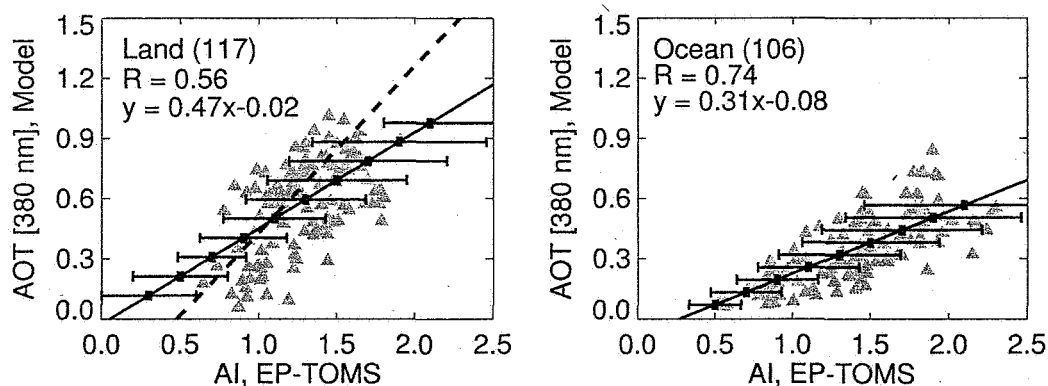
Figure 17. Scatterplots of monthly mean AOT₃₈₀ observed by EP-TOMS versus model. The domain is divided into two regions: land (left) and ocean (right). The dashed line represents the 1-to-1 line and the solid line represents the line of best fit.



1703 Figure 18. Scatterplots of monthly mean AOT₅₅₀ observed by MODIS versus MISR at points
 1704 over land (left) and ocean (right) for September 2000. The dashed line represents the 1-to-1 line
 1705 and the solid line represents the line of best fit.



1706
 1707
 1708 Figure 19. Scatterplots of monthly mean EP-TOMS AI versus simulated monthly mean AOT₃₈₀
 1709 for September 2000. The geographic domain is restricted to a region dominated by biomass
 1710 burning aerosols (5°S to 20°S and 10°W to 35°E) and then separated into land (left) and ocean
 1711 (right) points. The solid lines in both figures represent the line of best fit. The dashed line in land
 1712 plot represents the regression line from the comparison of AERONET AOT₃₈₀ and EP-TOMS AI
 1713 over smoke dominated locations in September 2000.



1714

Figure 20. Daily mean column-integrated volume size distribution simulated by the base model (solid line) and the daily mean column-integrated volume size distribution fitted to parameters from AERONET almucantar scans (dashed line) at Etosha Pan on 13 September 2000. The model size distribution is normalized to the fine volume concentration of the AERONET retrieval.

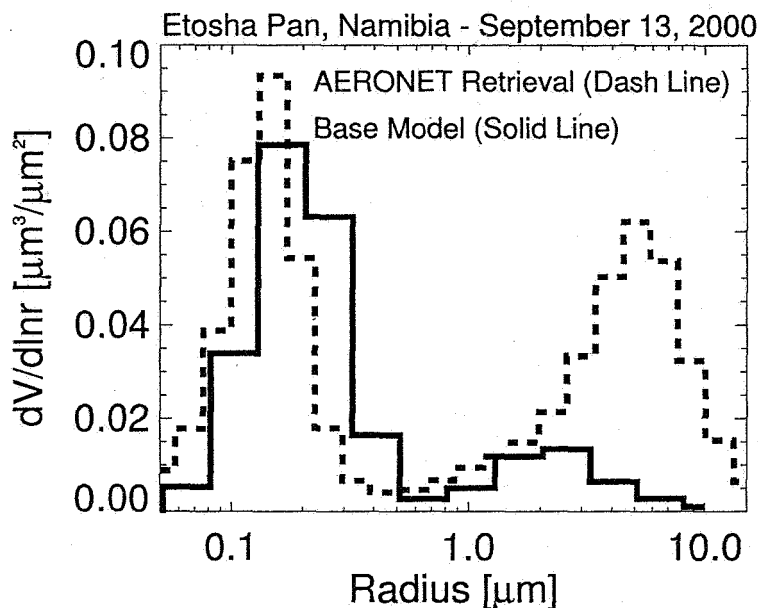


Figure 21. Daily mean volume size distribution simulated by the base model (solid line) and the volume size distribution fitted to parameters reported by *Haywood et al.* [2003] which are representative of average PCASP measurements within an aged smoke (dashed line) at Etosha Pan on 13 September 2000. The model size distribution is normalized to the fine volume concentration of the PCASP measurement.

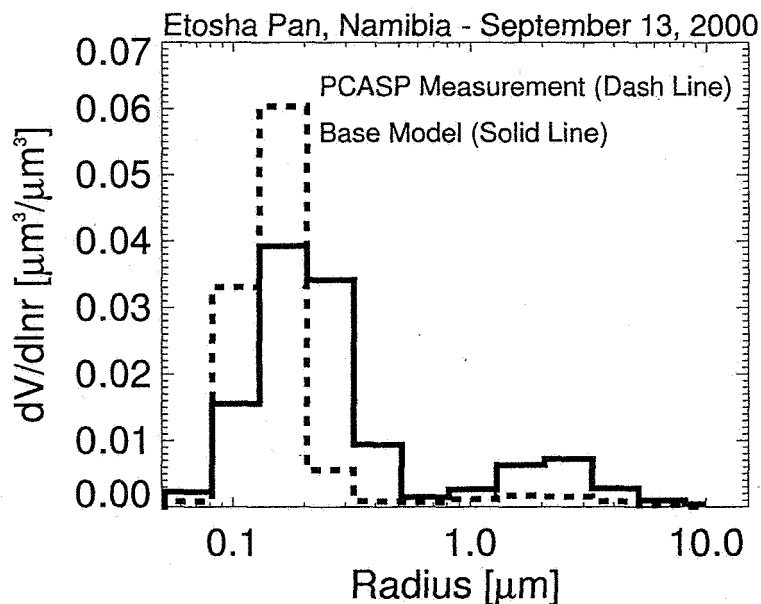


Figure 22. Normalized column-integrated daily mean volume size distributions at Ndola, Zambia on 16 September 2000. The model size distributions are normalized to the fine volume concentration of the AERONET retrieval. The black solid line represents the base model, gray solid line represents the PCASP model, and the dashed black line represents the AERONET retrieval.

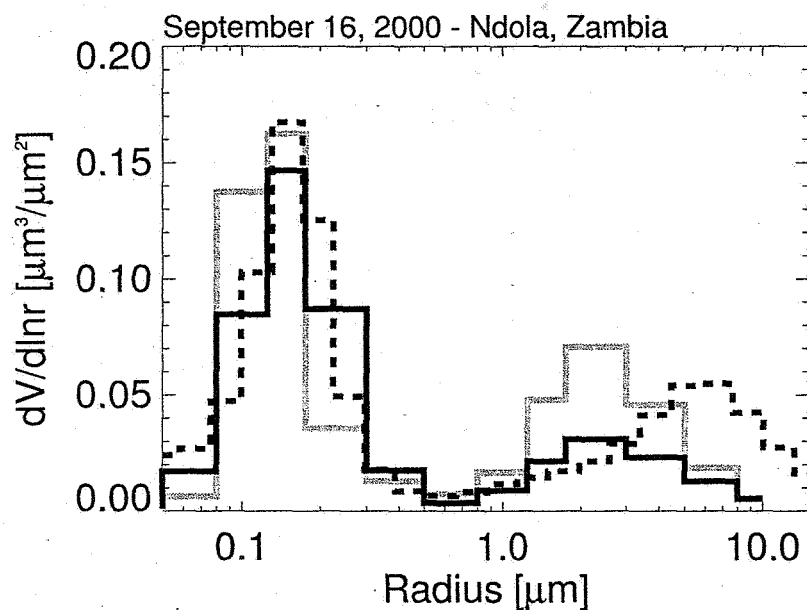


Figure 23. Normalized daily mean column-integrated AERONET and simulated volume size distributions at Ndola, Zambia on 16 September 2000. The model size distributions are normalized to the fine volume concentration of the AERONET retrieval. The solid black line represents the base model, gray line represents Density model, the gray dashed line represents the No Dry Dep. model, and the dashed black line represents the AERONET retrieval.

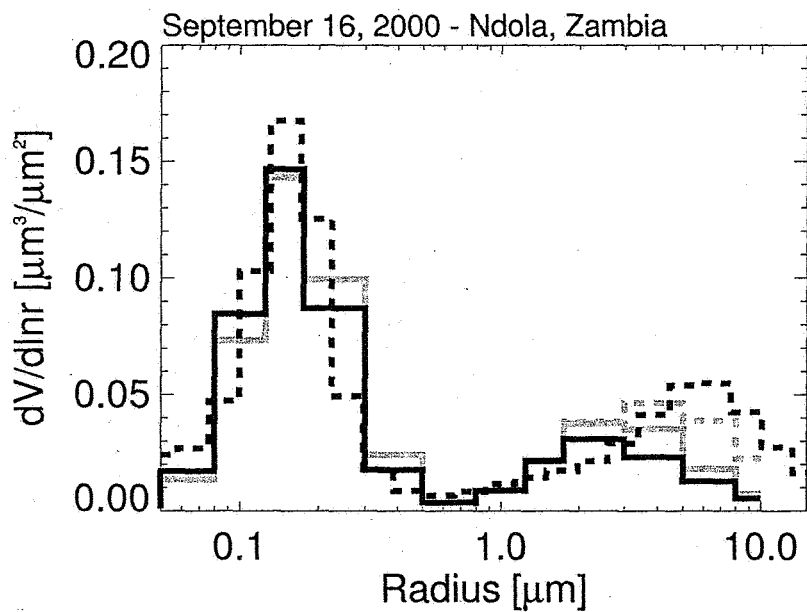


Figure 24. AERONET and simulated mean spectral dependence of SSA of smoke dominated days for September 2000 at Inhaca and Ndola. The solid line represents the results from the Base model, the dotted line represents the WD-AERONET model, the dashed-dotted line represents the WI-AERONET model, the dashed line represents the WD-AERONET-Mean model, and the asterisks connected with dashed line represent the AERONET retrievals.

